

Lateral/Directional Control Law Design and Handling Qualities Optimization for a Business Jet Flight Control System

Tom Berger*

University Affiliated Research Center, Moffett Field, CA

Mark B. Tischler†

U.S. Army Aviation Development Directorate-AFDD, Moffett Field, CA

Steven G. Hagerott‡

Cessna Aircraft Company, Wichita, KS

Dagfinn Gangsaas§

Nomaan Saeed¶

Aerospace Control Dynamics LLC, Minden, NV

Design of lateral/directional control laws for a business jet was performed using a two step optimization approach to meet a comprehensive set of stability, handling qualities, and performance specifications. First, a linear-quadratic regulator method was employed for preliminary design as a way to initialize the control law feedback gain values for optimization. Subsequently, a multi-objective parametric optimization approach was used to arrive at feed-forward and feedback gains that concurrently satisfy all specifications. The specifications were divided into two tiers. The first were the key flight control and handling qualities requirements and were used directly for optimization, while the second were used as a check afterwards. This paper describes the control law architecture used as well as the optimization approach, the specifications used, and the design results.

Nomenclature

α	Angle-of-attack [deg, rad]
\bar{q}	Dynamic pressure [psf]
β	Angle of sideslip [deg, rad]
β_{cg}	Angle of sideslip at airplane CG [deg, rad]
β_{cmd}	Commanded sideslip [deg]
β_{vt}	Angle of sideslip of vertical tail [rad]
δ_f	Rudder deflection [rad]
δ_a	Aileron actuator position [deg]
δ_{ped}	Pedal deflection
δ_r	Rudder actuator position [deg]
δ_{wheel}	Lateral stick deflection
η	Correction for flap effectiveness factor
ω_c	Crossover frequency [rad/sec]

*Research Engineer, University Affiliated Research Center, Senior Member AIAA.

†Flight Control Technology Group Leader, Senior Scientist, U.S. Army Aviation Development Directorate-AFDD, Associate Fellow AIAA.

‡Engineer Specialist, Cessna Aircraft Company, Senior Member AIAA.

§President, Aerospace Control Dynamics LLC., Associate Fellow AIAA.

¶Chief Engineer/VP, Aerospace Control Dynamics LLC., Member AIAA.

This material is declared a work of the U.S. Government and is not subject to copyright protection in the United States.

ω_n	Natural frequency [rad/sec]
$\omega_{b_{cmd}}$	Directional axis command model frequency [rad/sec]
ω_b	Directional axis LQR output shaping function frequency of complex-pair target zeros [rad/sec]
ω_{DR}	Dutch roll frequency [rad/sec]
ω_{inv}	Inverse model frequency [rad/sec]
ω_p	Lateral axis LQR output shaping function frequency of complex-pair target zeros [rad/sec]
ϕ	Roll attitude [deg, rad]
τ	Flap effectiveness factor, time delay [sec]
τ_{cmd}	Command time delay [sec]
$\tau_{p_{cmd}}$	Lateral axis command model time constant [sec]
θ	Pitch attitude [deg, rad]
ζ	Damping ratio [-]
$\zeta_{b_{cmd}}$	Directional axis command model damping [-]
ζ_b	Directional axis LQR output shaping function damping of complex-pair target zeros [-]
ζ_{DR}	Dutch roll damping [-]
ζ_{inv}	Inverse model damping [-]
ζ_p	Lateral axis LQR output shaping function damping of complex-pair target zeros [-]
a_b	Directional LQR output shaping function real zero [rad/sec]
c	Vertical tail chord length [ft]
C_l	Coefficient of lift on the vertical tail
C_{l_α}	Vertical tail lift curve slope [1/rad]
g	Acceleration due to gravity [ft/sec ²]
J_{LOES}	LOES fit cost
J_{MF}	Model following cost
K	Control law gain
L	Lift [lbs]
L_β	Dimensional rolling moment due to sideslip (dihedral) derivative [1/sec ²]
L_{δ_a}	Dimensional rolling moment due to aileron deflection derivative [rad/sec ² -deg]
L_{δ_r}	Dimensional rolling moment due to rudder deflection derivative [rad/sec ² -deg]
$L_{\dot{\beta}}$	Dimensional rolling moment due to sideslip rate derivative [1/sec]
L_r	Dimensional rolling moment due to yaw rate derivative [1/sec]
M	Vertical tail root bending moment [ft-lbs]
n_y	Lateral acceleration [g]
N_{δ_a}	Dimensional yawing moment due to aileron deflection derivative [rad/sec ² -deg]
N_{δ_r}	Dimensional yawing moment due to rudder deflection derivative [rad/sec ² -deg]
p	Roll rate [deg/sec, rad/sec]
p'	Lateral axis feedback [rad/sec]
p_s	Stability axis roll rate [rad/sec]
p_{cmd}	Commanded roll rate [deg/sec]
Q	LQR output shaping function weight [-]
R	LQR input shaping function weight [-]
r	Yaw rate [deg/sec, rad/sec]
r_s	Stability axis yaw rate [rad/sec]
s	Laplace variable
V	True airspeed [ft/sec]
x_{vt}	Longitudinal distance of vertical tail from CG [ft]
y	LQR output shaping function [-]
z	Distance up vertical tail from root [ft]
z_{vt}	Vertical distance of vertical tail from CG [ft]
CG	Center of Gravity
DRB	Disturbance Rejection Bandwidth
DRP	Disturbance Rejection Peak
EMF	Explicit Model Following
LOES	Lower Order Equivalent System
LQR	Linear-Quadratic Regulator

OLOP Open Loop Onset Point
PIO Pilot Induced Oscillation
RMS Root mean square

I. Introduction

A handling qualities optimization based approach to flight control design was previously used to generate a smooth gain schedule for longitudinal control laws with predicted Level 1 handling qualities.¹ The optimization was driven by a comprehensive set of specification divided into two tiers. This approach was motivated by several comprehensive compendiums of flight control design experience and lessons learned, which emphasize the importance of meeting multi-tier handling qualities and flight control criteria for improved safety (e.g. RTO,² Pratt³), and to avoid pilot induced oscillations (PIO) in the design phase.

This paper applies the same optimization based approach to lateral/directional control laws widely used in industry, using a model of a small business jet in nonterminal flight phase. As with the longitudinal control laws,¹ a linear-quadratic regulator (LQR) design method using target zeros employed by Gangsaas, et al,⁴ was utilized in a preliminary design phase to initialize control law gain values. This produced excellent initial conditions for the subsequent optimization. The gains were then directly optimized while including high order system effects such as time delays and actuator dynamics to satisfy the handling qualities and flight control requirements using a multi-objective parametric optimization algorithm. This resulted in the ability to optimize an entire gain schedule in a matter of hours with no manual tuning.

This paper first describes the aircraft for which this control system is designed. Next, a detailed description of the control laws is given, including a discussion of which elements in the control laws can be modified between flight conditions, or scheduled. After a brief description of the Control Designer's Unified Interface (CONDUIT[®]), the software used for control law optimization in this study, a description of the handling qualities specifications used is given. Then, the optimization strategy is discussed, including a detailed description of how LQR is used to initialize the gain values. Finally, the results are presented, first for one flight condition, and then for the entire gain schedule, followed by conclusions.

II. Aircraft Model

THE aircraft used in this study is a light business jet similar to the Cessna CitationJet 1 (CJ1), or Model 525, shown in Figure 1. It is a twin turbofan-powered business jet which can carry three to nine passengers. It has a maximum take-off weight (MTOW) of 10,700 lbs, a cruise speed of 389 KTAS, a maximum range of 1,300 nm, and a service ceiling of 41,000 ft. For this study, it is assumed that the ailerons and rudder are driven by hydraulic actuators, with a full authority fly-by-wire control system.



Figure 1. Typical light business jet—Cessna CitationJet 1 (CJ1), or Model 525.

A. Bare-Airframe Model

In order to produce meaningful analyses and develop a good control system, a comprehensive full flight envelope model of the aircraft dynamics is necessary. In this case, linear models of the aircraft at different Mach, flight altitude, weight, and center of gravity (CG) combinations were estimated using DARcorporation Advanced Aircraft Analysis software.⁵ Sixty-six different Mach and altitude combinations were considered, and at each of those design points, 13 different weight and CG combinations were considered, for a total of over 850 models. All models are for a flaps-up, gear-up cruise configurations, and are the same models used in the previous development of longitudinal control laws.¹ Figure 2(a) shows the different Mach and altitude combinations, as well as the aircraft flight envelope.⁶ Figure 2(b) shows the different weight and CG combinations, as well as the aircraft weight-CG envelope.⁶ Several weight/CG configurations which are outside the envelope were used in this analysis in order to design the control laws for additional robustness.

The variation due to Mach/altitude must be considered for the purpose of gain scheduling. Figures 3(a) and 3(b) show variations in the bare-airframe Dutch roll frequency and damping of the nominal weight/CG configuration as a function of Mach and inverse dynamic pressure. The plots are shown as a function of $40/\bar{q}$ instead of $1/\bar{q}$ to scale the x-axis around 0-1. The Dutch roll frequency increases with increasing dynamic pressure (decreasing $40/\bar{q}$) and is well grouped for different Mach values. Conversely, the Dutch roll damping varies both dynamic pressure and with Mach number. Additional examples of the variations of stability and control derivatives with loading and flight conditions are presented in Tischler and Remple.⁷ Due to these variations with both dynamic pressure and Mach, both parameters will be used to schedule the control law gains.

As the control law gains will not be scheduled with weight or CG, for the sake of simplicity, each Mach/altitude combination is treated as a design point with a nominal loading configurations (weight = 8500 lbs, mid-CG location) marked as “Nominal” on Figure 2(b), and two off-nominal weight and CG configurations, chosen to span the weight-CG envelope at each flight condition. The off-nominal weight and CG configurations were chosen at each flight conditions as those with the highest and lowest Dutch roll damping ratios. Figures 4(a) through 4(d) show the Dutch roll damping for all weight and CG configurations at four different flight conditions. The figures show that the off-nominal configurations with the highest and lowest Dutch roll damping vary with flight condition. At each flight condition, the two off-nominal loading configurations with the highest and lowest bare-airframe Dutch roll damping will be used in evaluating certain specifications to ensure control law stability and performance robustness to changes in weight and CG.

Special consideration must also be given to the frequency of the bare-airframe Dutch roll mode. This is because the control system’s ability to increase Dutch roll damping is largely dictated by the equivalent phase lag in the loop, which includes contributions from time delays, anti-aliasing and notch filters, actuators, etc. Since the control loop phase lag increases with frequency, it becomes increasingly more challenging to obtain good closed loop damping for higher frequency Dutch roll modes.

Circled on Figure 2(b) are the two off-nominal configurations chosen for the Mach 0.3, Sea Level flight condition: “Light”-weight = 6000 lbs, forward-CG with the highest Dutch roll damping ratio in this case, and “Heavy”-weight = 10,800 lbs, aft-CG with the lowest Dutch roll damping ratio in this case. Figures 5(a) and 5(b) show the range of roll rate and sideslip frequency responses for all weight and CG configurations (grey patches) at one point design (Mach 0.3, Sea Level). Highlighted on the plots are the responses for the nominal loading configurations and the two off-nominal loading configurations chosen for this flight condition (“Light”-weight = 6000 lbs, forward-CG and “Heavy”-weight = 10,800 lbs, aft-CG), which bracket the variations in the roll rate and sideslip responses for all the weight/CG configurations.

B. Vertical Tail Loads Model

In order to assess the effects of the control system on vertical tail loads (lateral shear, bending moment, and torsion), it is important to directly incorporate a vertical tail loads model in the design process. Load equations are generally provided by the Loads group, which have high fidelity load models, however for this analysis a simple bending moment model was developed based on 2D airfoil strip theory and several simplifying assumptions. The assumptions made are:

1. The lift curve slope of the vertical tail airfoil, C_{l_α} , is assumed to be constant throughout the flight envelope.

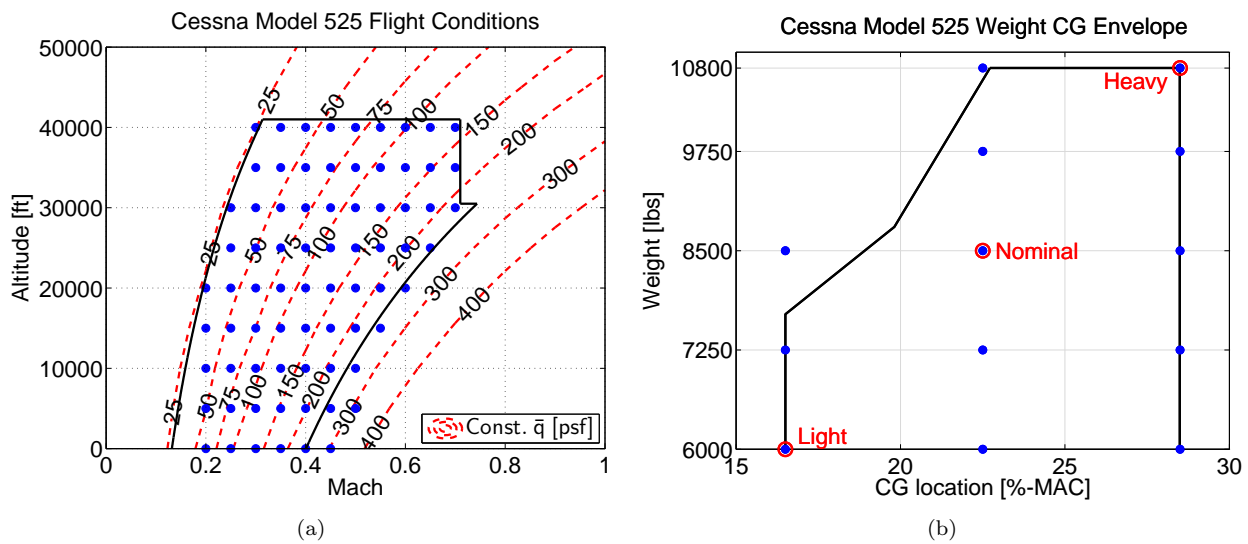


Figure 2. Aircraft (a) flight and (b) loading conditions and envelopes.

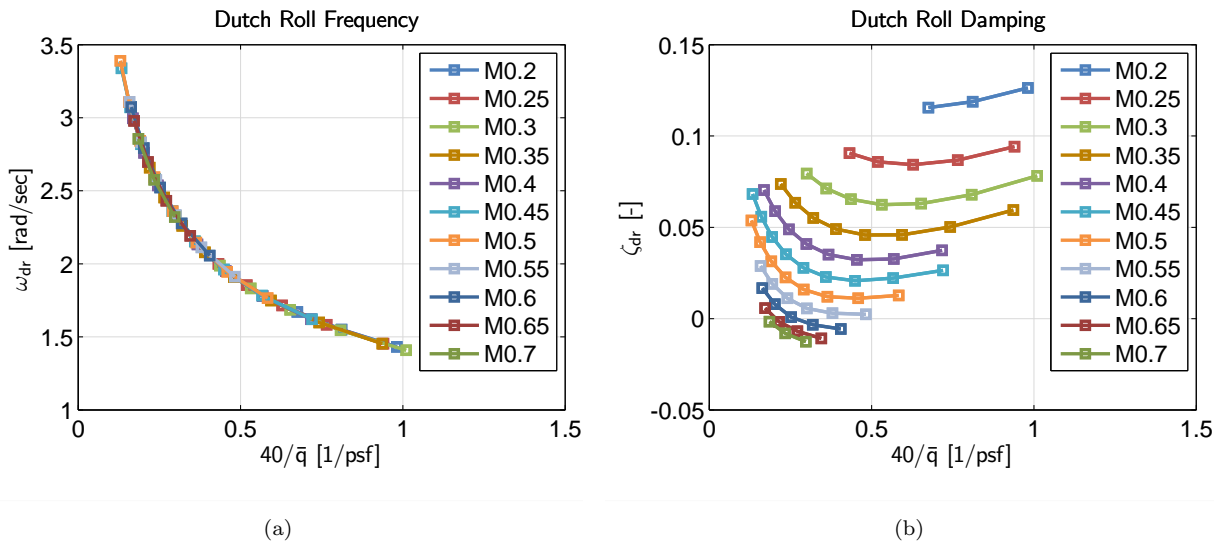
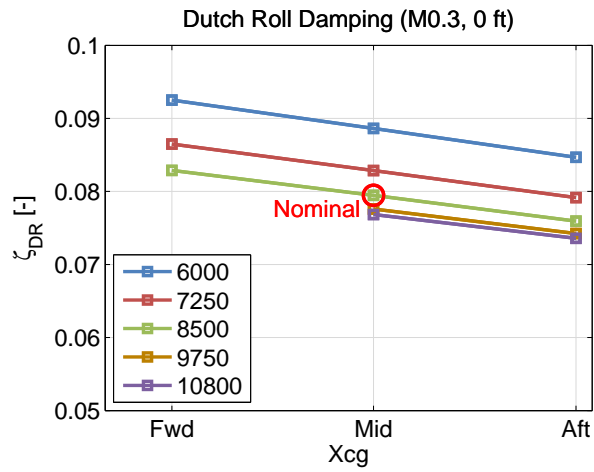
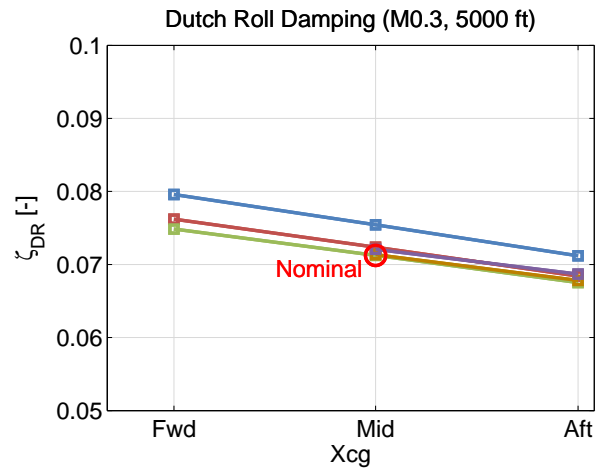


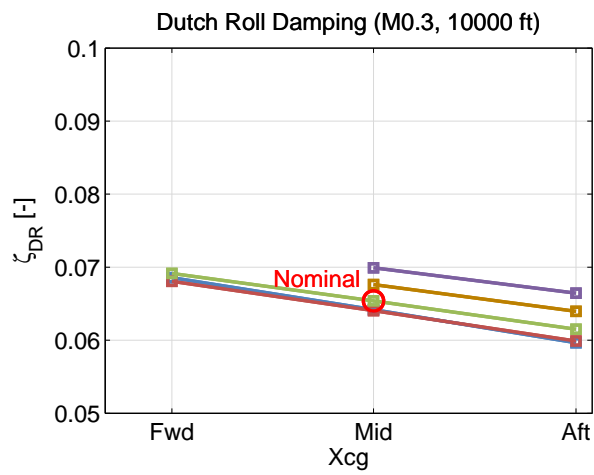
Figure 3. Variations in bare-airframe Dutch roll (a) frequency and (b) damping with Mach and inverse dynamic pressure (Nominal weight/CG).



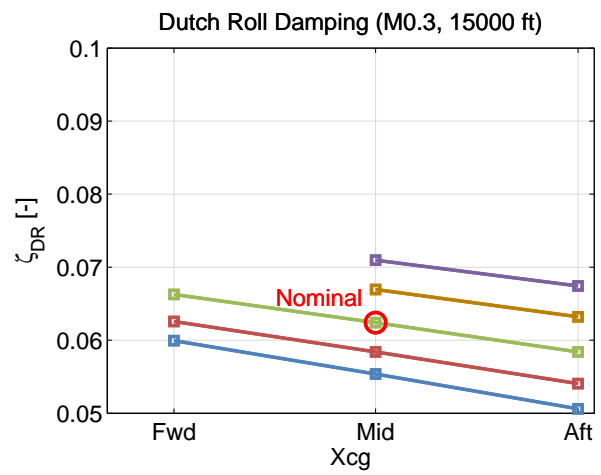
(a)



(b)



(c)



(d)

Figure 4. Variations in bare-airframe Dutch roll damping for different loading configurations at flight conditions (a) Mach 0.3, Sea Level, (b) Mach 0.3, 5000ft, (c) Mach 0.3, 10,000ft, and (d) Mach 0.3, 15,000 ft.

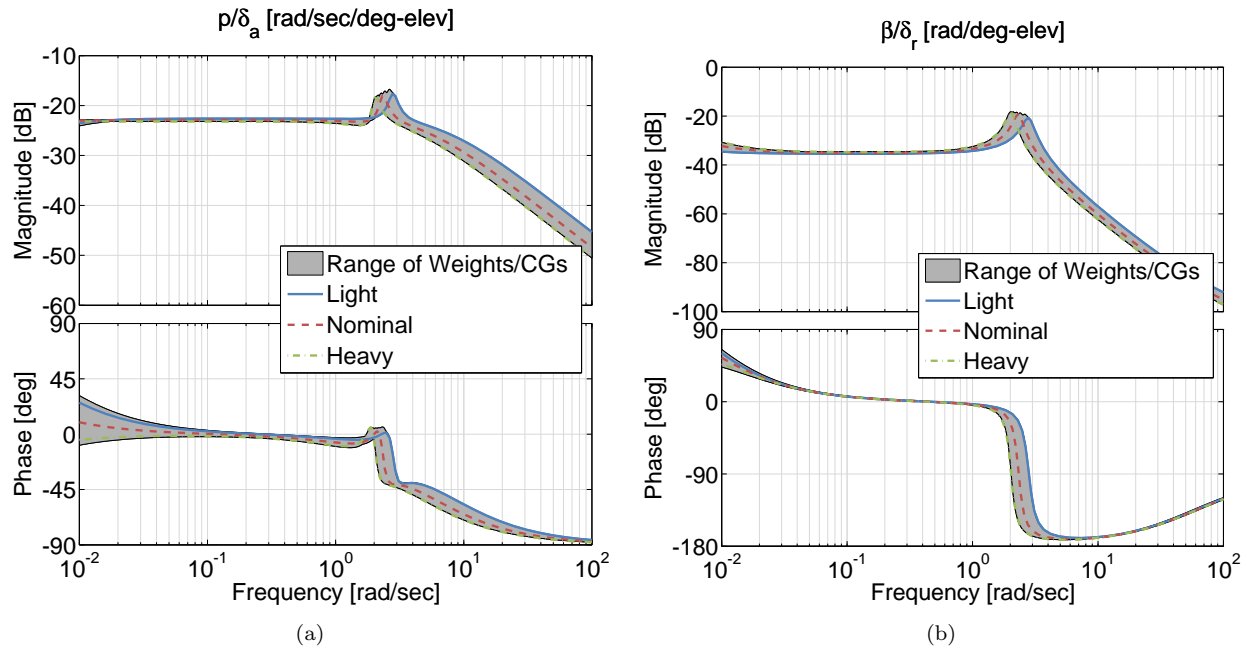


Figure 5. Range of (a) roll rate and (b) sideslip responses to appropriate inputs across the range of weight and CG configurations (Mach 0.3/Sea Level flight condition).

2. Tip vortices are neglected, due to the endplate effects of the fuselage below and the horizontal tail above the vertical tail. Therefore, only two dimensional flow over the vertical tail is considered.
3. Sidewash on the tail is neglected for this analysis.
4. Only lift acting on the vertical tail is used to calculate the moment at the vertical tail root.

A higher fidelity tail loads model could be developed, which takes into account sidewash and the fact that the horizontal tail and fuselage are not fully effective endplates by looking at the 3D vortex lattice, but such a model is outside of the scope of this paper. Furthermore, it important to look at the trade-off between all three vertical tail loads—lateral shear, bending moment, and torsion. However, for the purpose of this design only the bending moment is analyzed because it is the primary driver in sizing the tail cone structure.

The root bending moment of the vertical tail is determined by integrating the lift generated by each span-wise strip section of the tail multiplied by its moment arm from the root. First, an expression of the lift is required. The tail generates lift from its angle-of-attack (airplane sideslip) and flap deflection (rudder deflection). The coefficient of lift for a flapped airfoil is given as:⁸

$$C_l = C_{l_\alpha}(\alpha + \tau\eta\delta_f) \quad (1)$$

Where,

- C_{l_α} is the lift curve slope of the vertical tail airfoil,
- α is the angle-of-attack of the vertical tail,
- τ is the flap effectiveness factor,
- η is the correction for flap effectiveness factor, and
- δ_f is the rudder deflection.

The angle-of-attack of the vertical tail is the airplane sideslip at the tail, given by:⁷

$$\beta_{vt} = \frac{v - pz_{vt} + rx_{vt}}{V_0} \quad (2)$$

Positive sideslip generates lift on the tail in the negative y -direction. Therefore α in Equation 1 equals negative β_{vt} in Equation 2. Combining the two equations and integrating along the vertical tail span to get the total lift:

$$L = \int_{root}^{tip} \bar{q} c C_{l_\alpha} \left(-\beta_{cg} + \frac{p}{V_0} z_{vt} - \frac{r}{V_0} x_{vt} + \tau \eta \delta_{rud} \right) dz \quad (3)$$

Finally, in order to get a bending moment at the vertical tail root from the equation above, the force must be multiplied by the distance z from the tail root. Breaking up the integral, and moving variables that are not functions of z outside of the integral, the expression for the root moment becomes:

$$M = - \left(C_{l_\alpha} \int cz dz \right) \bar{q} \beta_{cg} + \left(C_{l_\alpha} \int cz z_{vt} dz \right) \bar{q} \frac{p}{V_0} - \left(C_{l_\alpha} \int cz x_{vt} dz \right) \bar{q} \frac{r}{V_0} + \left(C_{l_\alpha} \tau \eta \int cz dz \right) \bar{q} \delta_{rud} \quad (4)$$

Equation 4 gives the vertical tail bending moment as a function of constants dependent on the tail geometry, the aircraft flight condition and states, and rudder deflection.

This tail load model is also used to determine the maximum allowable load on the tail. The maximum load on the tail is assumed to be the root moment at maximum dynamic pressure and maximum sideslip defined by the operational flight envelope, with zero rudder deflection, roll rate, and yaw rate:

$$M_{max} = -865.56 (\bar{q} \beta_{cg})_{max} \quad (5)$$

From the flight envelope of the CJ1, the maximum dynamics pressure is assumed to be $\bar{q}_{max} = 300$ psf. The maximum angle-of-sideslip at that dynamic pressure is assumed to be $\beta_{cg_{max}} = 8$ deg. Therefore, the maximum root moment is $|M_{max}| \approx 36,000$ ft-lbs. This maximum tail load will be enforced as one of the specifications used during gain optimization.

III. Control Laws

THE control law architecture used in this study is referred to as “ $p - \beta$ ”-command, i.e. stability axes roll rate command in the lateral axis and sideslip command in the directional axis.^{9,10} The architecture is shown in simple form in Figure 6. The feed-forward paths in Figure 6, are comprised of the direct wheel to aileron path and a first-order pre-filter in the lateral axis, and a direct pedal to rudder path and a second-order pre-filter in the directional axis. These feed-forward paths are adjusted to meet the handling qualities requirements, while the feedback path, comprised of stability axes roll rate, sideslip, and sideslip rate, is used to meet the stability, damping, and gust rejection requirements. Cross-feed gains, from the directional axis feedback and feed-forward paths to the aileron actuator and from the lateral axis feedback and feed-forward paths to the rudder actuator, are used to tune the off-axis responses to meet handling qualities and gust rejection requirements.

As was done in the longitudinal axis,¹ a direct analogy was made between the control laws shown in Figure 6 and an explicit model following (EMF) control law architecture.¹¹ It is helpful to explore the similarities between these two control law architectures because EMF control laws assure that the end-to-end response follows the desired lower-order command model. This is useful for gain scheduling of the command model and feed-forward gains, as is done here and described in Section III.A.1. Moreover, a lower-order end-to-end response is desired, both for good handling qualities,⁴ and to ensure that the lower-order equivalent systems (LOES) specifications, described in Section V, accurately predict the handling qualities of the aircraft.

The Pre-Filter blocks in Figure 6 are used as the Command Models in each axis, and are covered in more detail in Section III.A.1. The feed-forward gains K_p , K_d , and K_{ff} take the place of inverse models in EMF control laws. Section VI.A will describe how these gains can be used to exactly construct a first-order inverse model in the lateral axis and a second-order inverse model in the directional axis, in order to achieve the full benefits of an EMF controller with the architecture used here.

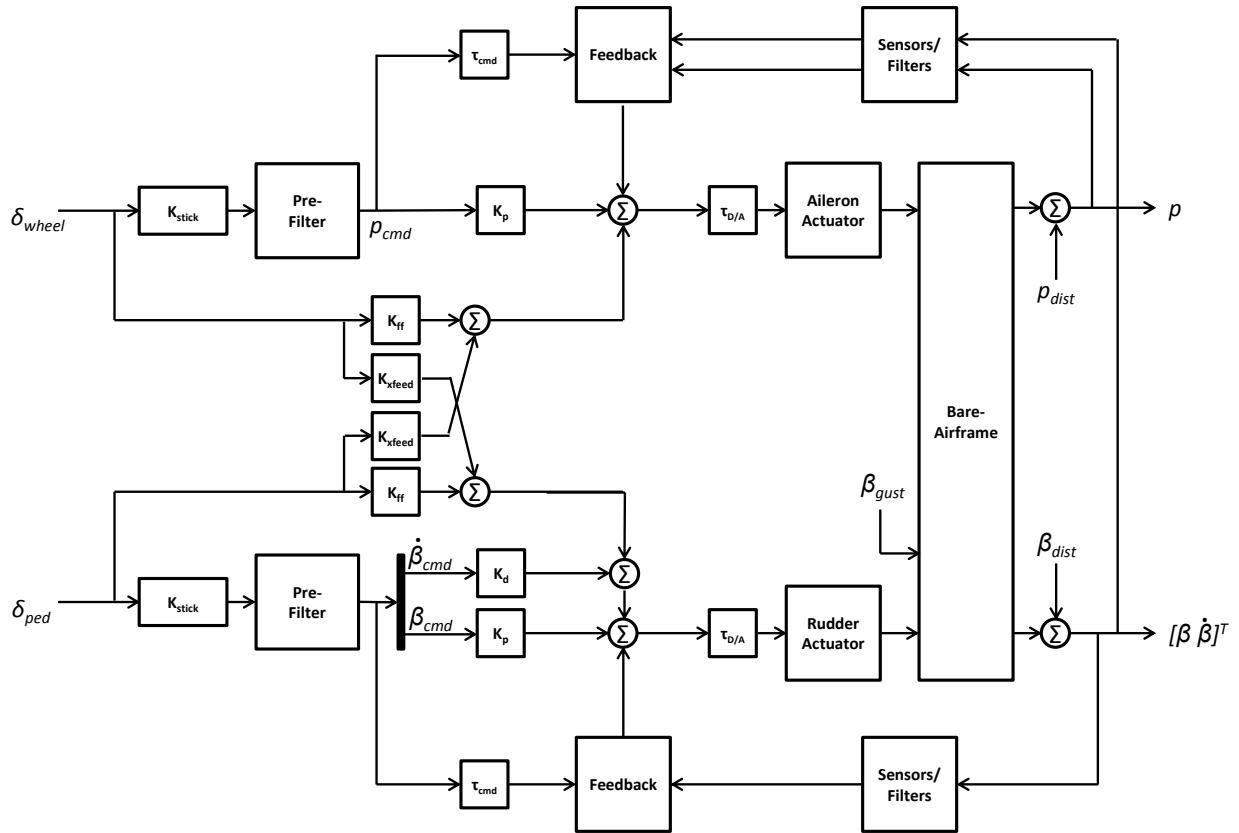


Figure 6. Schematic of typical lateral/directional control law block diagram (based on Gangsaas, et al⁴).

Command delays (τ_{cmd} in Figure 6), were included to enhance the control law's model following capabilities by synchronizing the command model and aircraft responses. The benefits of these delays are described in detail in the previous longitudinal control laws paper.¹

The remainder of this section will be broken down into the Design Parameters and Set Parameters of the block diagram. Design parameters are those that are determined either by hand tuning or through optimization, and are different for each flight condition. Set parameters are those which do not change with flight condition, and are frozen throughout the aircraft flight envelope.

A. Design Parameters

1. Feed-Forward

The first components of the feed-forward section of the control laws are the command models, sometimes referred to as a pre-filters. The command models represent the desired dynamics in each axis. In the lateral axis, a first-order command model is used, consistent with the order of the primary bare-airframe response:

$$\frac{p_{cmd}}{\delta_{wheel}} = \frac{1}{\tau_{p_{cmd}}s + 1} \quad (6)$$

While in the directional axis, a second-order command model is used:

$$\frac{\beta_{cmd}}{\delta_{ped}} = \frac{\omega_{b_{cmd}}^2}{s^2 + 2\zeta_{b_{cmd}}\omega_{b_{cmd}}s + \omega_{b_{cmd}}^2} \quad (7)$$

Where,

- $\tau_{p_{cmd}}$ is set equal to the bare-airframe roll mode time constant, τ_r
- $\zeta_{b_{cmd}} = 0.7$ to provide a well damped directional response, and
- $\omega_{b_{cmd}} = \omega_{dr}$ to retain the good inherent Dutch roll frequency of the bare-airframe aerodynamic design and to not overdrive the actuators.

Note that the bare-airframe roll mode time constant and Dutch roll frequency values in the command models are selected for the nominal weight/CG configuration at each flight condition.

2. Feedback

Feedback is used to minimize the error between the commanded stability axes roll rate and sideslip and actual aircraft responses, as well as to provide improved damping, stability, gust rejection, and robustness. This is done with proportional and integral (PI) paths in the lateral axis, and proportional, integral, and derivative (PID) paths in the directional axis, as well as cross-feed gains, as shown in Figure 7.

In the lateral axis, the quantity fed back and compared with commanded roll rate is a combination of stability axis roll rate and derivative of roll attitude:

$$p' = \frac{s}{s+a}p_s + \frac{a}{s+a}\dot{\phi} \quad (8)$$

where $a = 0.25$ rad/sec, and $\dot{\phi}$ is reconstructed from inertial measurements. This ensures that the wheel commands $\dot{\phi}$ in steady-state, and can be returned to the detent position for a steady turn with constant bank angle, even if the pitch attitude is not zero.

In the directional axis the quantity fed back and compared with commanded sideslip is sideslip and sideslip rate. Since there is no direct measurement of sideslip rate, it is reconstructed from inertial measurements:

$$\dot{\beta}_{inertial} = g \frac{n_y + \sin \phi \cos \theta}{U} - r_s \quad (9)$$

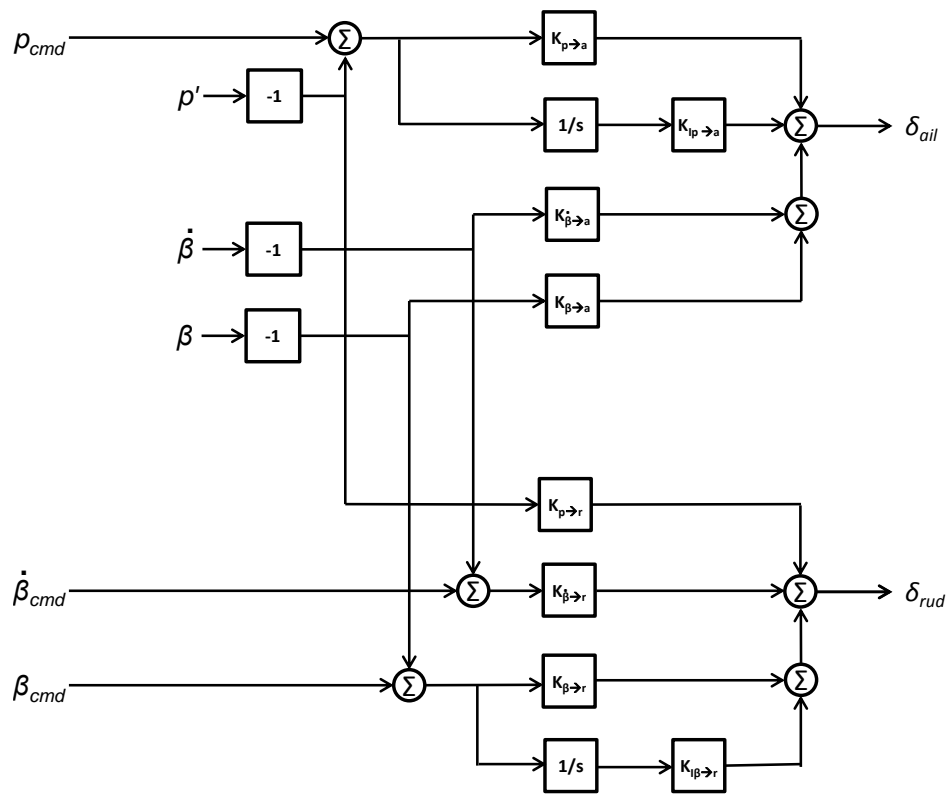


Figure 7. Schematic of the feedback block in the control law block diagram.

B. Set Parameters

1. Actuators

For the system modeled, the aileron and rudder actuators are represented as second-order systems with $\omega_n = 22.6$ rad/sec, $\zeta = 0.7$, position limits of ± 15 deg, and rate limits of 36 deg/sec.

2. Flight Control Computer Delay

Accounting for all sources of delays in the block diagram is important to accurately predict the stability and handling qualities characteristics of the control laws. The computation delay is set to half time-step ($\tau = 10$ msec) for the assumed 50 Hz flight control computer (FCC). Additionally, the digital-to-analog sample and hold delay is accounted for by a half time-step ($\tau = 10$ msec) delay upstream of each actuator.¹²

3. Sensors and Sample Delays

Sensors are modeled as second-order systems with frequencies of $\omega_n = 4.8$ Hz on angle-of-sideslip, $\omega_n = 8$ Hz on roll rate, yaw rate, and roll attitude, and $\omega_n = 6.4$ Hz on lateral acceleration. Additionally, each sensor signal has a $\tau = 20$ msec delay, to account for sampling skew and bus transport delays.¹²

4. Filters

The wheel and pedal input anti-aliasing filters are modeled as a first order 5 Hz lag.

Filters on the measured aircraft responses include a complementary filter on sideslip using sideslip rate reconstructed from inertial measurements, as shown in Equation 9.

The complementary filtered sideslip, β_{cf} , is built up such that:

$$\beta_{cf} = \underbrace{\frac{s}{s^2 + 2\zeta_{cf}\omega_{n_{cf}}s + \omega_{n_{cf}}^2} \dot{\beta}_{inertial}}_{\text{High-Frequency Contribution}} + \underbrace{\frac{2\zeta_{cf}\omega_{n_{cf}}s + \omega_{n_{cf}}^2}{s^2 + 2\zeta_{cf}\omega_{n_{cf}}s + \omega_{n_{cf}}^2} \beta_{measured}}_{\text{Low-Frequency Contribution}} \quad (10)$$

where,

$\dot{\beta}_{inertial}$ is sideslip rate reconstructed from inertial measurements (Equation 9),

$\beta_{measured}$ is the measured sideslip,

$\omega_{n_{cf}}$ is the complementary filter frequency, 0.25 rad/sec in this case, and

ζ_{cf} is the complementary filter damping, 0.7 in this case.

Figure 8 shows the contribution of reconstructed sideslip, $\beta_{inertial}$, and measured sideslip, $\beta_{measured}$ to the complementary filtered sideslip. As expected, the inertial and measured components sum to 1.0, as indicated by Equation 10 and Figure 8.

To properly capture all sources of the control law's phase lag, structural notch filters have also been included in the block diagram. In this example, notch filters were included on the sideslip rate feedback signal. For the purposes of this analysis, it is assumed that the complementary filter on the sideslip signal provides inherent high-frequency attenuation, and therefore notch filters are not required for that signal. Sample structural mode notch filters for this class of aircraft could include notches at $\omega_n = 5, 10,$ and 15 Hz, which have been used for the notch filters in this analysis. The damping ratio for the numerator and denominator notch filter terms are $\zeta_{num} = 0.05$ and $\zeta_{den} = 0.5$, respectively, which set the depth and width of each filter. These notch filters are assumed for this control law and aircraft to provide aeroservoelastic stability, which requires 9 dB of gain margin from control law structural coupling.¹³ However, an aeroservoelastic stability analysis that includes the coupled aircraft and structural dynamics is required for production control law design, but is out of scope for this analysis.

A lead-lag filter is also added downstream of the notch filters to help recover some of the phase loss associated with the notches. This was necessary in order to meet the damping ratio specification for some of the higher dynamic pressure flight conditions. The lead-lag filter was hand tuned using several of the corner cases of the flight envelope. The trade-off between the added phase lead at the cost of more high-frequency gain (which can reduce gain margin) from the lead-lag filter is shown in Figure 9.

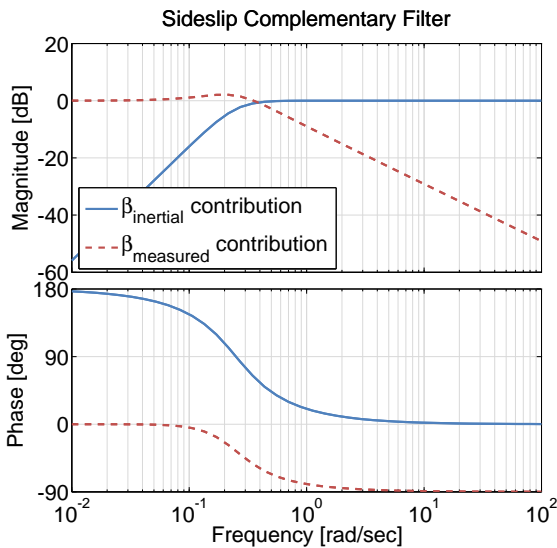


Figure 8. Complementary filtered sideslip contributions.

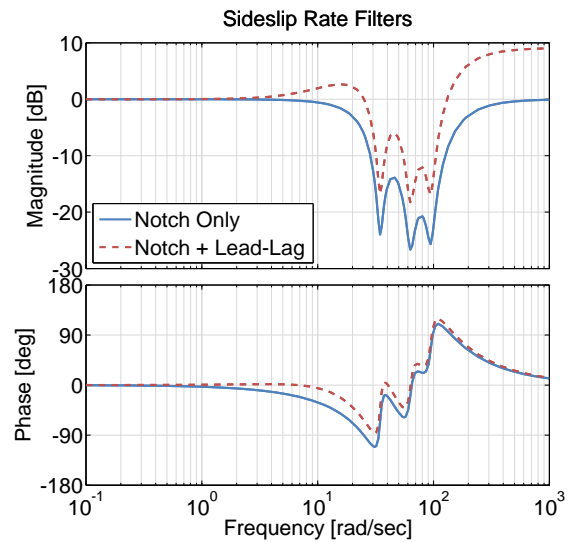


Figure 9. Filters on sideslip rate.

5. Turbulence, Gusts, and Disturbances

Finally, for the purpose of evaluating the control laws gust and turbulence loads performance,¹⁴ a Dryden turbulence model,¹⁵ as well as discrete 1-cosine sideslip gust model¹⁴ have been integrated into the block diagram. These are included through an additional input to the bare-airframe state-space model, a B_{gust} matrix, which is comprised of only the aerodynamic terms (no Coriolis or gravity terms) of the bare-airframe state-space model A matrix. Disturbances in each response are summed into the output of the bare-airframe block.

IV. Control Designer's Unified Interface

THE control laws described in the previous section were analyzed and optimized using the Control Designer's Unified Interface (CONDUIT[®]).^{16,17} CONDUIT[®] is a commercial software tool developed by the U.S. Army Aviation Development Directorate–AFDD in conjunction with the University Affiliated Research Center, University of California, Santa Cruz. It leverages MATLAB[®] to evaluate a Simulink block diagram against a defined set of stability, handling qualities, and performance specifications, and performs a multi-objective parametric optimization of user defined parameters in the block diagram (e.g. feedback gains) in order to meet those specifications, while minimizing the cost of feedback (actuator usage and noise sensitivity).

V. Specifications

A comprehensive set of stability, handling qualities, and performance specifications was chosen to drive the optimization of the control laws. The handling qualities specifications are based on MIL-STD-1797B¹⁵ and engineering judgement, and the required stability margins are based on the military specification for flight control systems, MIL-DTL-9490E.¹³ As was done in the longitudinal axis,¹ the specifications were divided into two categories—First Tier and Second Tier specifications. First Tier specifications are key flight control and handling qualities requirements that drive the design optimization. They are evaluated at each iteration of the control law optimization and are guaranteed to be met for an optimized design. Second Tier specifications are those which are evaluated only at the end of the optimization. Because they are not evaluated during the optimization, due to computational time consideration, they are not always met. However, they are evaluated for the final optimized designs to ensure they are not grossly violated. There is generally sufficient overlap between the First Tier and Second Tier specifications, such that the Second Tier specifications are also met or are close to being met by the optimization process.

A. First Tier Specifications

First Tier specifications are used to drive the optimizations and are divided into three constraint types in CONDUIT[®]. Specifications that ensure aircraft stability, such as the eigenvalue, stability margin, and Nichols margin specifications, are categorized as *hard constraints*. These specifications are met during the first phase of optimization, and cannot be violated in subsequent phases of the optimization. The stability and Nichols margin specifications were evaluated for the loops broken at both the aileron and rudder actuators (input robustness). Additional Nichols margin specifications were evaluated for the loops broken at the roll rate, yaw rate, lateral acceleration, and sideslip sensors (output robustness).

The next subset of First Tier specifications contains the handling qualities specifications, which are categorized as *soft constraints* and are met during the second phase of optimization. These specifications include the LOES specifications of MIL-STD-1797B: roll mode time constant and Dutch roll damping and frequency. As this analysis was done for up-and-away flight conditions and a medium weight aircraft, the Category B, Class II-L boundaries were used for the MIL-STD-1797B LOES specifications.

In addition to the MIL-STD-1797B LOES specifications, four more LOES specifications were included in the optimization. Inclusion of the first two additional LOES specifications enforces the costs of the LOES fits⁷ of roll rate to aileron input to be $J_{LOES} \leq 10$ and sideslip to rudder input to be $J_{LOES} \leq 20$. A higher cost was allowed for the sideslip response since it is higher order, however, this is still a very low cost. Enforcing these low costs ensures that the aircraft responds as a lower order system and that the parameters of the LOES fit very accurately capture the closed-loop dynamics of the aircraft. The third and fourth additional LOES specifications ensure that the Dutch roll frequency and roll mode time constant of the LOES fits are within $\pm 20\%$ and $\pm 30\%$, respectively, of their bare-airframe values. The inclusion of these LOES specifications prevent over driving of the actuators, by limiting how much the control system can augment the bare-airframe modes.

The LOES fits used here are individual fits of the roll rate response to wheel input and sideslip response to pedal input. The fits were made over the frequency range of 0.1-10 rad/sec, and the LOES transfer functions are given below:⁷

$$\frac{p}{\delta_{wheel}} = \frac{K_p e^{-\tau_p s}}{s + 1/\tau_r} \quad (11)$$

$$\frac{\beta}{\delta_{pedal}} = \frac{K_b e^{-\tau_b s}}{s^2 + 2\zeta_{dr}\omega_{dr}s + \omega_{dr}^2} \quad (12)$$

Two individual fits are used, instead of a simultaneous fit, since the responses are decoupled by design.

The remaining handling qualities specifications do not require a LOES fit. The model following cost specifications compare the closed-loop stability axes roll rate and sideslip frequency responses with the frequency responses of the commanded roll rate and sideslip. A cost function similar to a LOES cost is computed based on the difference in the magnitude and phase of the responses. The comparison is done over the frequency range of 0.1-10 rad/sec. In the lateral axis, a cost of $J_{MF} \leq 50$ was enforced for the nominal aircraft configuration, whereas a cost of $J_{MF} \leq 100$ was enforced for off-nominal configurations. As with the LOES cost specification, a higher cost was allowed in the directional axis. These cost values are consistent with guidelines for system identification of lower order equivalent models.⁷

The next specification is the eigen-damping specification. This specification evaluates the damping ratio of all closed-loop eigenvalues within a specified frequency range and compares them to the minimum required value. The minimum damping ratio requirement is a function of frequency:

$$\zeta \geq \begin{cases} 0.4 & \omega_n \leq 10 \text{ rad/sec} \\ 0.3 & \omega_n > 10 \text{ rad/sec} \end{cases} \quad (13)$$

Meeting this requirement ensures that the linear response of the aircraft to both piloted and gust inputs are well damped, and that there are no lightly damping high-frequency modes.

The Open Loop Onset Point (OLOP) specification¹⁸ is included to evaluate the control law's susceptibility to Category II Pilot Induced Oscillations (PIOs). Category II PIOs are characterized by rate or position limiting. The OLOP specification examines actuator rate limiting, which has been the cause of several high profile accidents.¹⁸ Linear analysis methods ignore the non-linear effects of position and rate limiting.

However, the OLOP specification is based on frequency domain describing function concepts, and is useful to include in the design process to not push the design beyond the limits of the real aircraft.

Additional First Tier specifications concerned with ride quality are disturbance rejection bandwidth and peak.¹⁹ Disturbance rejection is assessed by evaluating the loop sensitivity function, i.e.:

$$\frac{\beta}{\beta_{dist}} = \frac{1}{1 + GH} \quad (14)$$

In this case, disturbance rejection was assessed for the sideslip response, as shown in Equation 14, as well as for the roll rate response. The Disturbance Rejection Bandwidth (DRB) metric is defined as the frequency where the magnitude curve of the sensitivity function frequency response crosses the -3 dB line. This is the frequency below which the control system can adequately reject disturbances and is a measure of the quickness of the system to recover from a disturbance. The Disturbance Rejection Peak (DRP) metric is defined as is the peak magnitude of the sensitivity function frequency response, and is a good measure of response overshoot for disturbance inputs. Figure 10 shows an example disturbance rejection response with its associated DRB and DRP.

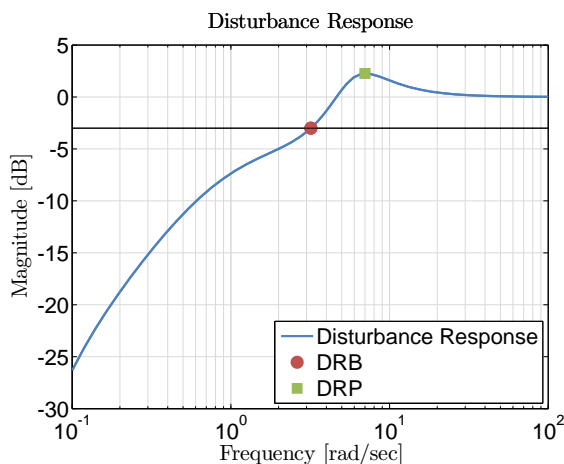


Figure 10. Example Disturbance Rejection Bandwidth (DRB) and Disturbance Rejection Peak (DRP).

First Tier specifications concerned with tail loads are the gust response and the tail root moment specifications. The gust response specification evaluates the lateral acceleration response of the aircraft to a 1-cosine sideslip gust, given by:

$$\beta_{gust} = \frac{K_g}{2} (1 - \cos(\omega_g t)), \quad 0 \leq t \leq 2\pi/\omega_g \quad (15)$$

where,

$$K_g = 5 \text{ deg, and}$$

$$\omega_g = \omega_{dr}.$$

The specification determines the resulting lateral acceleration response and ensures that the second peak is less than or equal in magnitude to the first peak.

The tail root moment specification evaluates the tail load directly (using the model developed in Section II.B) for a rudder kick maneuver, a 1-cosine sideslip gust (Equation 15), and for turbulence (using the Dryden Turbulence Model). Meeting this specification ensures that the tail load does not exceed the maximum value calculated in Section II.B.

Two minimum crossover frequency specifications are included in the optimization, as well, for both the lateral and directional axes. These specifications ensure that the frequency responses broken at the aileron and rudder actuators have a crossover frequencies $\omega_c \geq 3.5$ rad/sec. Setting the minimum crossover frequency is an alternate way to ensure the control system is robust to off-nominal configurations, rather than explicitly including many off-nominal models in the evaluation of every specification, which is computationally intensive

for optimization. It is especially useful in model following control law architectures such as this one, since most of the other handling qualities specifications can be met with a properly tuned command model and little feedback. Preliminary design, rules of thumb (e.g. Tischler, et al¹⁷), company history, or a trade-off study¹ are good ways to determine the appropriate value for minimum crossover.

The final group of First Tier specifications are used for performance optimization. These are categorized as *summed objectives*, and CONDUIT[®] minimizes these after all other specifications have been met. In this case, the two specifications included in this category are crossover frequency and root mean squared (RMS) actuator displacement for roll rate and sideslip disturbance input. Minimizing crossover frequency and actuator usage has many benefits including minimizing potential for spillover of control energy to high-frequency modes that can excite structural dynamics, improved stability margin robustness to uncertainty in aircraft dynamics, minimizing closed-loop sensitivity to noise, and minimizing potential actuator saturation and susceptibility to PIO. These specifications are referred to as the “cost of feedback” specifications, and the best design is the one that meets all of the stability and handling qualities requirements with the minimum cost of feedback.¹⁷

Note that the crossover frequencies in both the lateral and directional axes cannot be reduced below the 3.5 rad/sec that is enforced by the minimum crossover frequency soft objective requirements. As a result, the final optimized designs will have crossover frequencies that are on or just above that value.

B. Second Tier Specifications

Second Tier specifications are checked at the end of the design process, but are not evaluated during the optimization, in order to reduce optimization times. These specifications include the MIL-STD-1797B specifications on roll axis and yaw axis equivalent time delay, sideslip excursion, and roll oscillation. A roll PIO specification from MIL-STD-1797B, which is an extension of the Smith-Geddes criteria to the lateral/directional axis, is also included. In addition, the Innocenti lateral tracking criteria is included.²⁰

A Second Tier specification on turn coordination is included which is based on Cessna guidance. This specification requires the steady-state lateral acceleration during a steady turn to be $|n_y| \leq 0.015$ g.

An additional specification used to look at the decoupling of the Dutch roll response from the aircraft’s roll response is the roll rate transfer function zero cancellation specification. This specification evaluated the distance on the s-plane between the complex pair of zeros in the roll rate response and the Dutch roll mode poles, and compares it against a given tolerance. When the zeros lies directly over the poles, the Dutch roll response is eliminated from the roll response of the aircraft.

These specifications are not guaranteed to be met for the optimized design, but sufficient overlap between these specifications and the First Tier specifications generally ensures that they are met. When Second Tier specifications are not met in the design process, they can be moved to the First Tier and used to drive the optimization to ensure they are met. Similarly, when First Tier specifications are found to not drive the design, they can be moved to the Second Tier to minimize computation time.

C. Specification Summary

Table 1 lists the full set of First Tier and Second Tier specifications, as well as a brief description and source for each. The table also shows the weight/CG configurations used to evaluate each specification, which is described in more detail in Section VI.

VI. Optimization Strategy

AT each Mach/altitude flight condition, a multi-model point optimization was performed. The multi-model optimization includes off-nominal models (marked as “Light” and “Heavy” on Figure 2(b)) with variations in weight and CG at each Mach/altitude flight condition. Therefore, the multiple models used are each at the same flight condition, but with a different aircraft weight and CG position, which ensures that the worst case bare-airframe Dutch roll damping is included. As shown in Table 1, the off-nominal models were used to evaluate the stability and Nichols margin specifications. Additionally, the model following specifications in both the lateral and directional axes were evaluated for the off-nominal models using relaxed boundaries.

Table 1. Optimization Specifications

Constraint	Spec Name	Description (Motivation)	Domain*	Source	Config.**
<i>First Tier</i>					
Hard	EigLcG1	Eigenevalues in L.H.P. (Stability)	S	Generic	N
	StbMgG1	Gain and phase margins loop broken at actuators and sensors (Stability)	F	MIL-DLT-9490E	L,N,H
	NicMgG1	Nichols Margins loop broken at actuators and sensors (Stability)	F	GARTEUR	L,N,H
Soft	FrqRoD4	Roll model time constant (HQ)	L	MIL-STD-1797B	N
	FrqDrD3	Dutch roll frequency (ω_{dr}) (HQ)	L	MIL-STD-1797B	N
	DmpDrD2	Dutch roll damping (ζ_{dr}) (HQ)	L	MIL-STD-1797B	N
	ReaDrD2	$\zeta_{dr}\omega_{dr}$ (HQ)	L	MIL-STD-1797B	N
	FrqRoC1	$\tau_r \pm 30\%$ open-loop (HQ, Act. Activity)	L	Generic	N
	FrqDrC1	$\omega_{dr} \pm 20\%$ open-loop (HQ, Act. Activity)	L	Generic	N
	CosLoG1	Max LOES Cost (HQ)	L	Generic	N
	EigDpG1	Eigenvalue Damping (HQ, Loads)	S	Generic	N
	OlpOpG1	Open Loop Onset Point (PIO)	F	DLR	N
	ModFoG2	Command model following cost (HQ)	F	Generic	L,N,H
	GstRpG1	Sideslip gust response (Loads)	T	Generic	N
	DstBwG1	Dist. Rej. Bandwidth (Loads, Ride Quality)	F	ADS-33E	N
	DstPkG1	Dist. Rej. Peak (Loads, Ride Quality)	F	ADS-33E	N
	MaxMgT1	Maximum tail loads during rudder kick, gust, and turbulence (Loads)	T	Generic	N
	CrsMnG1	Minimum $\omega_c \geq 3.5$ rad/sec (Robustness)	F	Generic	N
Summed	CrsLnG1	Crossover Frequency (Act. Activity)	F	Generic	N
Obj.	RmsAcG1	Actuator RMS (Act. Activity)	F	Generic	N
<i>Second Tier</i>					
Check Only	TdlRoD1	Roll axis equivalent time delay (HQ)	L	MIL-STD-1797B	-
	TdlYaD1	Yaw axis equivalent time delay (HQ)	L	MIL-STD-1797B	-
	OscRoD4	Roll oscillations (HQ)	T	MIL-STD-1797B	-
	CouRsD2	Sideslip excursion (HQ)	T	MIL-STD-1797B	-
	PioRoD1	Roll PIO criteria (HQ)	T	MIL-STD-1797B	-
	TrnCrC1	Turn coordination (HQ)	T	Cessna	-
	OscRoD7	Roll rate transfer function zero cancellation	S	Generic	-
	InnRoD1	Innocenti lateral tracking	F	Innocenti	-

* F = Frequency domain specification, T = Time domain specification, L = LOES specification, S = s-plane

** N = Nominal weight/CG configuration only, L,N,H = Light, Nominal, and Heavy weight/CG configurations

A. Feed-Forward Gains

1. On-Axis

As described in Section III, the control laws used in this study, shown in Figure 6, are analogous to explicit model following control laws. The difference between the control architecture used in this study and model following control laws is that the feed-forward gains in each axis take the place of the Inverse Models. However, these gains can be used to exactly construct a first-order inverse model of the aircraft in the lateral axis and a second-order inverse model in the directional axis. The inverse models are determined by fitting the lower order SISO transfer function models:

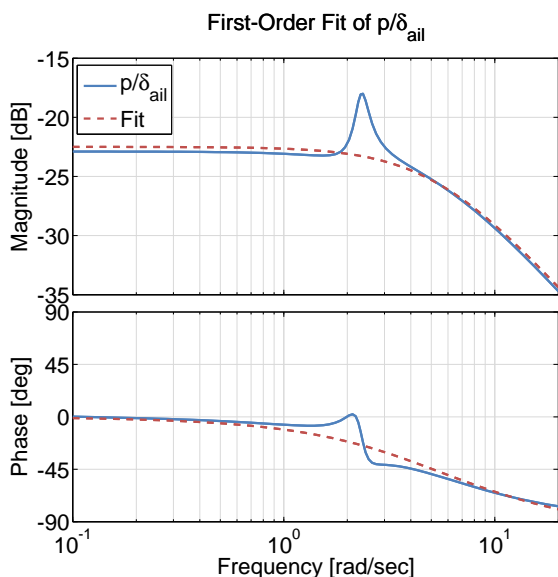
$$\frac{p}{\delta_{ail}} = \frac{K_{p_{inv}} e^{-\tau_{p_{inv}} s}}{s + 1/\tau_{p_{inv}}} \quad (16)$$

$$\frac{\beta}{\delta_{rud}} = \frac{K_{b_{inv}} e^{-\tau_{b_{inv}} s}}{s^2 + 2\zeta_{b_{inv}} \omega_{b_{inv}} s + \omega_{b_{inv}}^2} \quad (17)$$

to the on-axis responses of the bare-airframe, and then inverting them.

The fit is done over a frequency range from 0.1-20 rad/sec. Figures 11 and 12 show the roll rate and sideslip responses of the bare-airframe for one of the flight conditions, as well as their transfer function fits. Equation 18 shows the p/δ_{ail} transfer function and associated fit cost. As can be seen from Figure 11, the LOES SISO model does not capture the coupling of the Dutch roll dynamics. This is acceptable because when the feedback loops are closed, the Dutch roll response is both better damped and decoupled from the roll response.

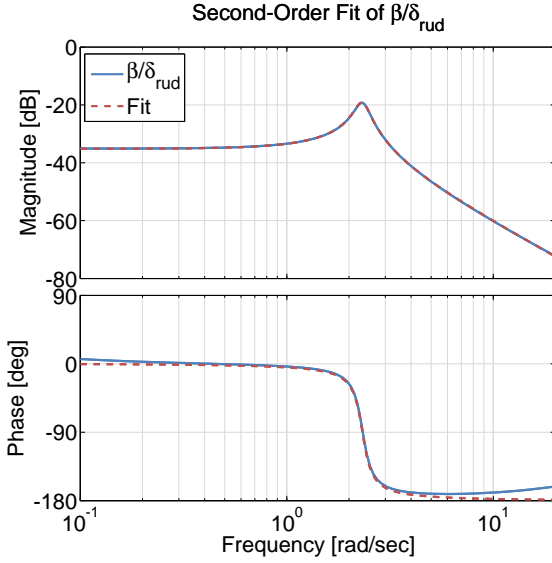
Equation 19 show the β/δ_{rud} transfer functions and associated excellent fit cost, indicating a very good model.



$$\frac{p}{\delta_{ail}} = \frac{0.3955e^{(-0.0036s)}}{(s + 5.275)} \quad (18)$$

0.1 - 20 rad/sec, Cost = 33.5

Figure 11. Inverse model fit of roll rate response (Mach 0.3/Sea Level flight condition; Nominal weight/CG).



$$\frac{\beta}{\delta_{rud}} = \frac{0.09407}{(s^2 + 2(0.07864)(2.324)s + (2.324)^2)} \quad (19)$$

0.1 - 20 rad/sec, Cost = 1.627

Figure 12. Inverse model fit of sideslip response (Mach 0.3/Sea Level flight condition; Nominal weight/CG).

Once the parameters of the inverse models are known, they can be used along with the command model parameters (given in Section III.A.1) to determine values for the feed-forward gains in each axis. In the lateral axis:

$$K_{p_p} = (1/\tau_{p_{inv}} - 1/\tau_{p_{cmd}})/(K_{p_{inv}}/\tau_{p_{inv}}) \quad (20)$$

$$K_{ff_p} = (1/\tau_{p_{cmd}})/(K_{p_{inv}}/\tau_{p_{inv}}) \quad (21)$$

and in the directional axis:

$$K_{p_\beta} = (\omega_{b_{inv}}^2 - \omega_{b_{cmd}}^2)/K_{b_{inv}}\omega_{b_{inv}}^2 \quad (22)$$

$$K_{d_\beta} = (2\zeta_{b_{inv}}\omega_{b_{inv}} - 2\zeta_{b_{cmd}}\omega_{b_{cmd}})/K_{b_{inv}}\omega_{b_{inv}}^2 \quad (23)$$

$$K_{ff_\beta} = \omega_{b_{cmd}}^2/K_{b_{inv}}\omega_{b_{inv}}^2 \quad (24)$$

Note that care has to be taken when determining the directional axis feed-forward gains for bare-airframes with an unstable Dutch roll mode (i.e. negative $\zeta_{b_{inv}}$). For those cases, the inverse plant poles are mirrored into the left-half plane, and $\zeta_{b_{inv}}$ remains positive. This still results in a good inverse model, since the directional feedback loop stabilizes the Dutch roll mode. Doing this prevents right-half plane zeros in the design due to the feed-forward gains.

2. Cross-Feed

Cross-feed gains in the feed-forward path are used to tune the off-axis responses to stick and pedal inputs. Initial values were selected for these gains to remove non-minimum phase zeros from the off-axis responses. This was done by considering the ratios of the proper dimensional control derivatives, as is commonly done for aileron-to-rudder interconnects. In this case, the values were scaled by appropriate feed-forward gain:

$$K_{ff_p \rightarrow rud} = K_{ff_p} \begin{pmatrix} -N_{\delta_a} \\ N_{\delta_r} \end{pmatrix} \quad (25)$$

$$K_{ff_\beta \rightarrow ail} = K_{ff_\beta} \begin{pmatrix} -L_{\delta_r} \\ L_{\delta_a} \end{pmatrix} \quad (26)$$

However, final tuning of the feed-forward cross-feed gains is generally done using simulator testing with pilots in the loop to determine what magnitude of off-axis responses are required for good handling qualities.

B. Feedback Gains

1. On-Axis

Feedback gains are optimized by CONDUIT[®] to meet the many specifications described in Section V, while minimizing actuator RMS and crossover frequency. Note however, that the crossover frequency has an enforced minimum value of 3.5 rad/sec. To increase convergence speed, it is important to have a good initial guess of the feedback gain values, especially when optimizing a large number of cases for an entire gain schedule. Initial values for the feedback gains are determined in preliminary design using the LQR method employed by Gangsaas, et al,⁴ which will be described here in detail.

The first step in the LQR optimization is to generate a lower order synthesis model. The LQR synthesis model only includes the aircraft dynamics, as well as the aileron and rudder actuator dynamics and lateral and directional command model dynamics and two output shaping functions. This model excludes the sensors, filters, and additional time delays included in the full block diagram.

Beginning with the three degree of freedom model of the bare-airframe rigid-body dynamics ($\mathbf{x} = [\beta \ p \ r \ \phi]^T$), the actuator dynamics are added to the system. The actuators are modeled as two second order system with $\omega_n = 22.6$ rad/sec, $\zeta = 0.7$, and results in the following state vector: $\mathbf{x} = [\beta \ p \ r \ \phi \ \delta_{ail} \ \dot{\delta}_{ail} \ \delta_{rud} \ \dot{\delta}_{rud}]^T$. Next, a change of variable is made transforming the yaw rate state to sideslip rate using a similarity transformation ($\mathbf{x} = [\beta \ p \ \dot{\beta} \ \phi \ \delta_{ail} \ \dot{\delta}_{ail} \ \delta_{rud} \ \dot{\delta}_{rud}]^T$).

The command models, shown in Equations 6 and 7, are then included in the synthesis model. Additionally, an integral error state is added in the directional axis given by:

$$\int err = \int (\beta_{cmd} - \beta) \quad (27)$$

The second component of the synthesis model is made up of both the lateral and directional output shaping functions. The shaping functions, given by:

$$y_p = \frac{(s^2 + 2\zeta_p\omega_p s + \omega_p^2)}{s} p \quad (28)$$

$$y_b = \frac{(s + a_b)(s^2 + 2\zeta_b\omega_b s + \omega_b^2)}{s} \beta \quad (29)$$

are weighted by the LQR algorithm. They set target zeros close to the locations of the desired closed-loop poles, i.e., desired roll mode and Dutch roll dynamics. In this case, a second-order shaping function on roll rate and a third-order shaping function on sideslip are used, where ζ_p , ω_p , a_b , ζ_b , and ω_b set the target zeros. Generally, the target zeros are treated as tuning knobs, and would be varied accordingly for each design point. However, in this case, since the LQR approach is used only to initialize the CONDUIT[®] feedback gain optimization, the target zeros are fixed for all cases at:

$$\omega_p = 1/\tau_r \quad (30)$$

$$\zeta_p = 1.0 \quad (31)$$

$$a_b = \omega_{dr} \quad (32)$$

$$\omega_b = \omega_{dr} \quad (33)$$

$$\zeta_b = 0.7 \quad (34)$$

where,

τ_r is the roll mode time constant of the nominal weight/CG bare-airframe at each flight condition, and

ω_{dr} is the Dutch roll frequency of the nominal weight/CG bare-airframe at each flight condition.

These target zeros ensure that the closed-loop flight dynamics frequencies are close to the good bare-airframe response, but with improved damping. Additionally, they ensure that the roll and yaw axis integrator gains are of sufficient magnitude for most applications.

With the target zeros fixed, the remaining tuning knobs become the LQR weighting on the shaping function, Q , and control weighting matrix, R . Since there are two shaping function used here and two

controls, both Q and R are 2x2. The LQR solution then gives the feedback gain from each of the synthesis model states to each of the two controls. Note that the resulting feedback gains on the actuator states are generally very small and are dropped.

Beginning with small values for the diagonal elements of Q , the crossover frequency is evaluated for the bare-airframe roll rate response with the LQR feedback gains K_p and K_ϕ . While the crossover frequency is less than 3.5 rad/sec (the target crossover frequency), the value of the LQR weighting matrix Q is increased, and the crossover frequency is re-evaluated. The resulting gains at the end of this very rapid iterative process are used as the initial guess for the CONDUIT[®] optimization.

In order to reduce the number of free parameters that the optimizer has to vary (both to reduce optimization time and avoid correlation issues), the integral gain in the directional axis was constrained to the proportional gain such that their ratio would be equal to 1/5 of the nominal crossover $\omega_c = 3.5$ rad/sec:

$$\frac{K_{I_\beta}}{K_\beta} = \frac{\omega_c}{5} \quad (35)$$

This ensures good low-frequency response tracking with minimum stability margin degradation due to the integral function, and has been employed for both inner- and outer-loop optimizations in the past.^{17,21}

It is possible to free the integral gain in the directional axis, although to avoid insensitivity issues,¹⁷ this would require the inclusion of a specification that is affected by this gain. An example of such a specification is a time domain steady-state turn coordination specification, or a steady-state tracking error specification in the presence asymmetric yaw input such as a single engine failure. However, time domain specification are computationally intensive, especially when run for a long simulation time as is the case for a steady-state error specification, so this was avoided for this design study. In the lateral axis, constraining the integral gain was not necessary, as it is an integral gain on a rate signal and not an attitude signal.

2. Cross-Feed

The cross-feed gains in the feedback path are used to eliminate contributions of the off-axis responses in the on-axis responses, and have also been constrained in this case. In the lateral axis, the cross-feed gains (i.e. $K_{\beta \rightarrow ail}$ and $K_{\dot{\beta} \rightarrow ail}$) are used to eliminate the Dutch roll response from the roll response, which is given by:

$$\dot{p} = L_p p + L_{\delta_{ail}} \delta_{ail} + L_\beta \beta + L_{\dot{\beta}} \dot{\beta} + L_{\delta_{rud}} \delta_{rud} \quad (36)$$

Note that a state transformation is used to convert the yaw rate state r to sideslip rate $\dot{\beta}$, and therefore the roll rate response in Equation 36 contains an $L_{\dot{\beta}}$ derivative instead of the more traditional L_r derivative.

For pure lateral pilot input, the rudder is only actuated through the directional feedback loop, and is approximated by:

$$\delta_{rud} = -K_{\beta \rightarrow rud} \beta - K_{\dot{\beta} \rightarrow rud} \dot{\beta} \quad (37)$$

Note that for simplicity, this approximation ignores the integral sideslip feedback gain as well as the feed-forward cross-feed gain.

Therefore, the roll rate response can be re-written as:

$$\dot{p} = L_p p + L_{\delta_{ail}} \delta_{ail} + (L_\beta - K_{\beta \rightarrow rud} L_{\delta_{rud}}) \beta + (L_{\dot{\beta}} - K_{\dot{\beta} \rightarrow rud} L_{\delta_{rud}}) \dot{\beta} \quad (38)$$

The contributions of sideslip and sidlip rate from the roll rate response can be negated by feeding those quantities back to the aileron with the following gains:

$$K_{\beta \rightarrow ail} = -\frac{(L_\beta - K_{\beta \rightarrow rud} L_{\delta_{rud}})}{L_{\delta_{ail}}} \quad (39)$$

$$K_{\dot{\beta} \rightarrow ail} = -\frac{(L_{\dot{\beta}} - K_{\dot{\beta} \rightarrow rud} L_{\delta_{rud}})}{L_{\delta_{ail}}} \quad (40)$$

Which are the augmented aircraft's L_β and $L_{\dot{\beta}}$. These cross-feed gains are frozen at their values during each iteration of the optimization based on the optimization's value for the on-axis directional gains $K_{\beta \rightarrow rud}$ and $K_{\dot{\beta} \rightarrow rud}$. In the directional axis, the cross-feed gain (i.e. $K_{p \rightarrow rud}$) is determined in a similar way.

Several of the specifications mentioned in Section V ensure the proper selection of the cross-feed gains. The First Tier model following cost specifications in both the lateral and directional axes ensure that the on-axis responses in each axis match their lower-order command models. In the lateral axis, the Second Tier roll rate transfer function zero cancellation specification evaluates the elimination of the Dutch roll response from the roll response of the aircraft by examining the distance on the s-plane between the complex pair of zeros in the roll rate response and the Dutch roll mode poles. Proper selection of the cross-feed gain results in lower-order on-axis responses and near cancellation of the Dutch roll response in the roll rate response.

VII. Results

A. Point Optimization

The point optimization results shown in this section are for the Mach 0.3, Sea Level flight condition. Figures 13(a) and 13(b) show the evolution of the predicted crossover frequencies in the lateral and directional axes, respectively, during the LQR initialization phase. As described in the previous section, the LQR weighting is increased until the lateral crossover frequency exceeds the 3.5 rad/sec threshold. Figures 14(a) through 14(e) show the evolution of the feedback gains during the LQR initialization phase, which runs instantaneously in MATLAB[®]. Note that only on-axis feedback gains are shown here for the sake of brevity, however, the gain schedule in Section VII.B is given for all feed-forward and feedback gains. The gain values at the end are then used to initialize the CONDUIT[®] optimization.

Figures 15(a) through 15(e) show the evolution of the design parameter values throughout the CONDUIT[®] optimization, illustrating the gain changes made by the optimizer beyond the initialized LQR solution to meet all of the handling qualities specifications. The CPU time to run the 19 iteration to complete the optimization takes roughly 10 minutes. As the figures show, the design parameters cease to vary in the last three iterations, which is the criteria to stop the optimization.

Once the optimized solution is reached, a sensitivity analysis is done on the design parameters.¹⁷ Figures 16(a) and 16(b) show the insensitivities and Cramer-Rao bounds of the design parameters, respectively. All insensitivities are well below 20%, meaning that each design parameter affects at least one of the active specifications. Furthermore, the Cramer-Rao bounds are all less than 40%, indicating that none of the design parameters are correlated with each other, and that the parameters are determined with good reliability. These good insensitivities and Cramer-Rao bound values indicate a well posed optimization problem statement.¹⁷

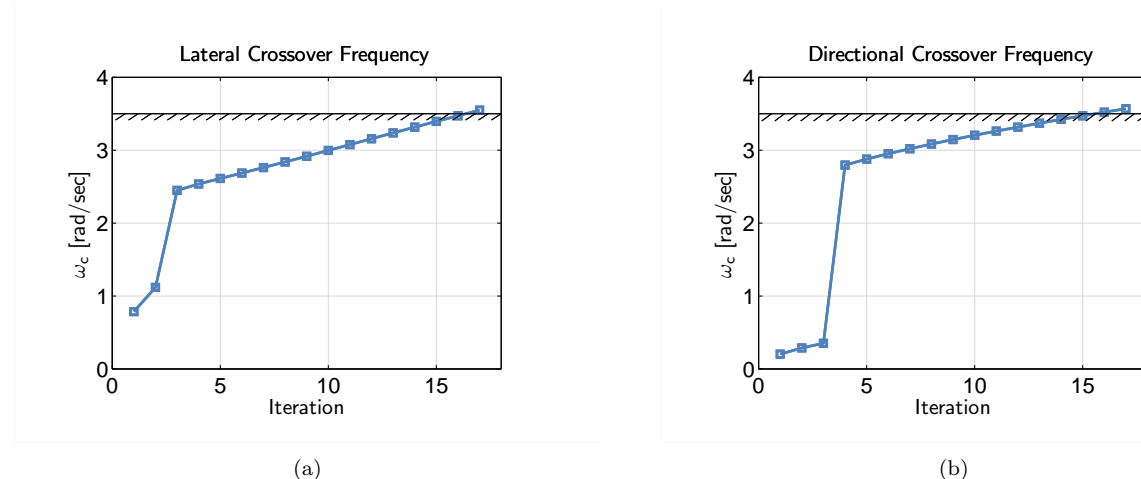
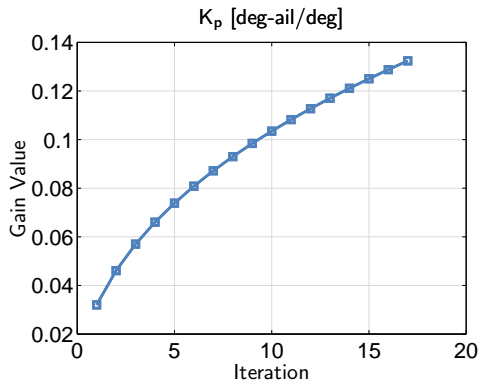
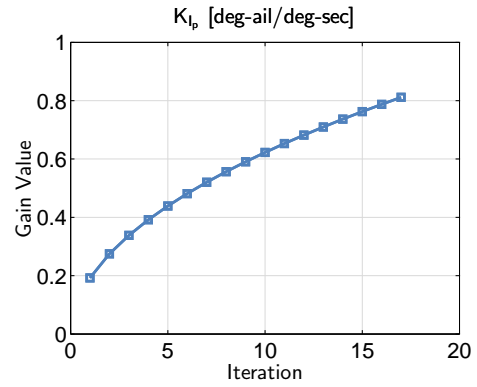


Figure 13. Variation in (a) lateral and (b) directional crossover frequencies with LQR iteration (Mach 0.3/Sea Level optimization).

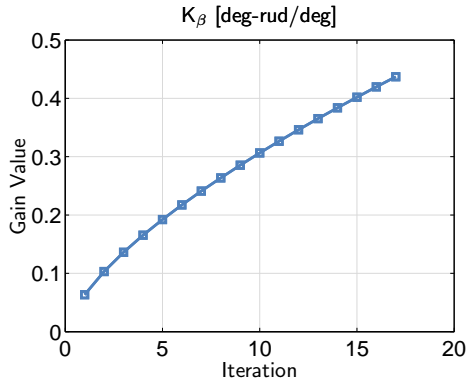
Figures 17 and 18 show the handling qualities window for the optimized design. All of the First Tier



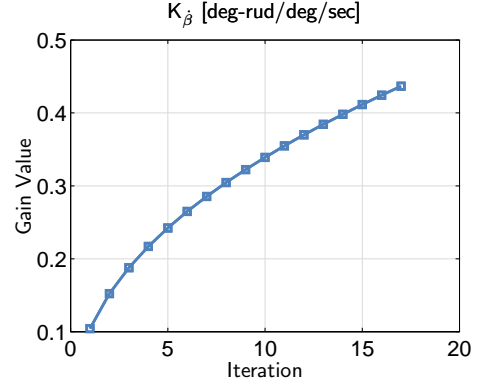
(a)



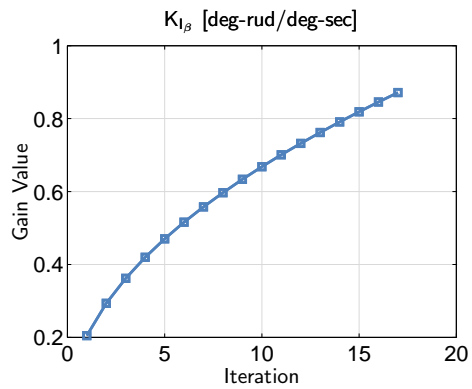
(b)



(c)

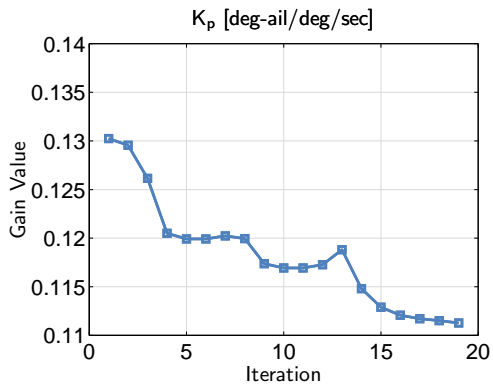


(d)

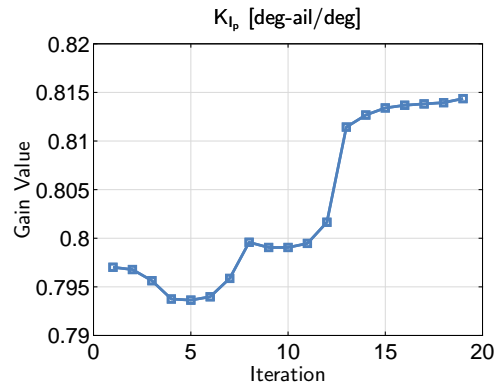


(e)

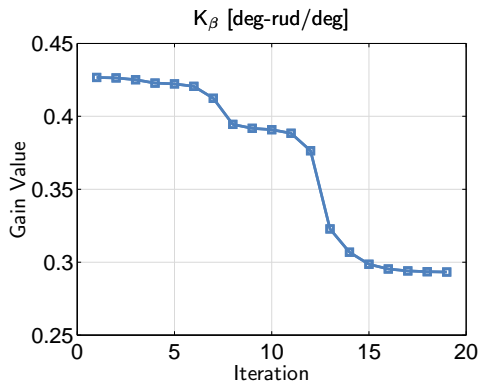
Figure 14. Variation in feedback gain values with LQR iteration (Mach 0.3/Sea Level optimization).



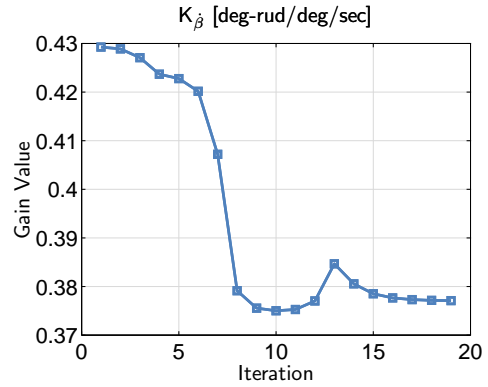
(a)



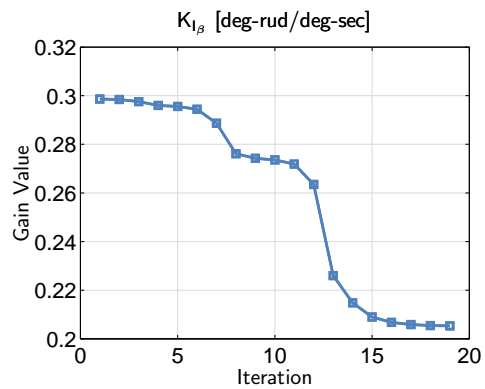
(b)



(c)



(d)



(e)

Figure 15. Design parameters variation with CONDUIT[®] iteration (Mach 0.3/Sea Level optimization).

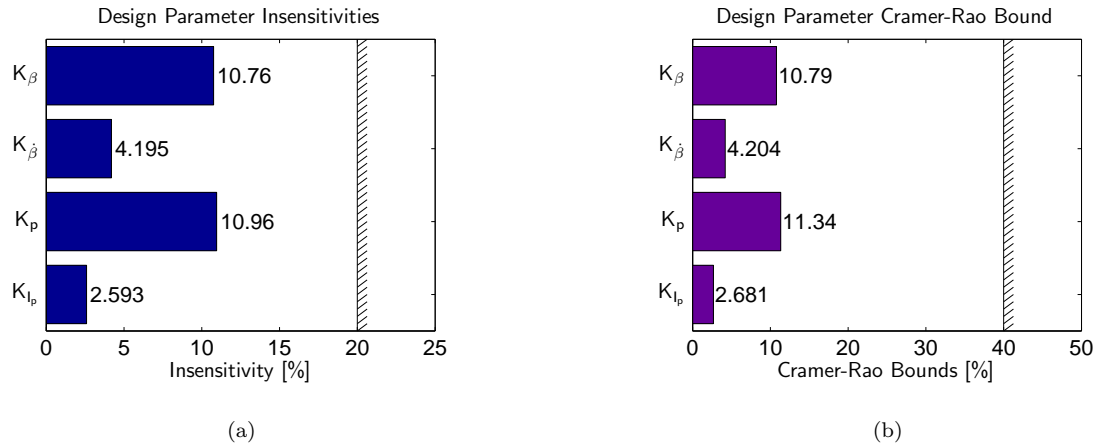


Figure 16. Design parameters (a) insensitivities and (b) Cramer-Rao Bounds (Mach 0.3/Sea Level optimization).

specifications are met within the design procedure. Several of the specifications are on the boundary, which is the solution that meets the requirements with the minimum “cost of feedback.” In addition, the Second Tier specifications, which are not enforced but checked, are also met, with the exception of the Innocenti lateral tracking criteria and equivalent roll time delay, which just cross their respective Level 1/Level 2 boundaries.

Figures 19 and 20 show the broken-loop responses of the optimized nominal weight/CG configuration at the aileron and rudder actuators, respectively. The responses both have the specified design crossover of $\omega_c = 3.5$ rad/sec and sufficient stability margins. Figure 21 shows the lateral axis model following of the aircraft. On the figure are plotted the roll rate command response (black line), as well as the stability axes roll rate responses of the closed-loop system for the nominal and two off-nominal (Light and Heavy) weight/CG configurations. The model following cost of the response, calculated over the frequency range of interest for handling qualities taken as 0.1-10 rad/sec (red arrow on Figure 21), is $J_{MF} = 1.2$ for the nominal configuration, which indicates an excellent match between the command model and the aircraft response. Beyond 20 rad/sec, the aircraft response diverges from the commanded roll rate response due to the presence of actuators, filters, and time delays in the closed loop system, which are not accounted for by the lower-order inverse model (as described in Section VI.A). Inclusion of these parameters in the inverse model is avoided because it would result in over driving the actuators, and instead they are accounted for with the command delays (Section III). The model following costs for the off-nominal configurations are $J_{MF} = 44.4$ for the Light configuration and $J_{MF} = 19.2$ for the Heavy configuration. These values are below the specification value of $J_{MF} \leq 100$ for off-nominal configurations and indicate that model following is robust to weight/CG changes in the bare-airframe.

Figure 22 shows the directional axis model following of the aircraft. On the figure are plotted the sideslip command response (black line), as well as the sideslip responses of the closed-loop system for the nominal and two off-nominal (Light and Heavy) weight/CG configurations. As in the lateral axis, there is excellent model following in the sideslip response in the frequency range of interest for handling qualities.

In order to assess the stability robustness at this point design, Nichols plots of the responses broken at multiple places in the loop are evaluated for the all weight and CG configurations. Figures 23 and 24 show the responses of the loop broken at the aileron and rudder actuators, respectively. All configurations avoid the exclusion zone (shown in gray),²² indicating robust stability. Figures 25 through 28, show the responses of the loop broken at the roll rate, yaw rate, lateral acceleration, and sideslip sensors, respectively. As with the loops broken at the actuators, all configurations avoid the exclusion zone, indicating robust stability.

Figure 29 shows the Dutch roll pole locations for all weight/CG configurations at this point design. The nominal weight/CG configuration is above the $\zeta \geq 0.4$ boundary of the minimum damping ratio specification. The forward CG configurations are better damped, due to the increased static directional stability. The aft CG configurations are slightly less damped, with the heavy-aft configuration having the lowest damping, $\zeta = 0.47$, which is still above the minimum damping requirement.

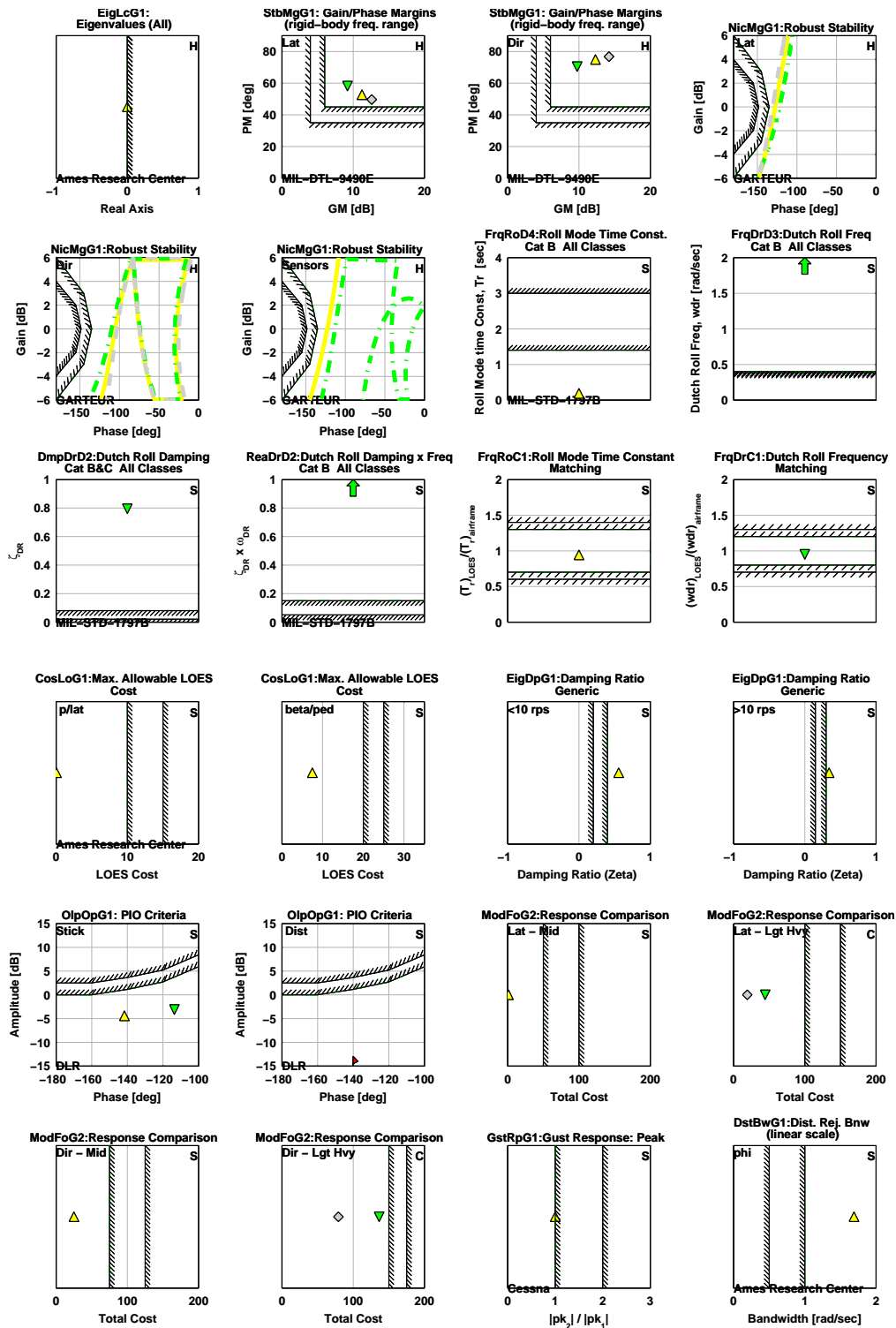


Figure 17. Handling qualities window of the optimized design (1/2) (Mach 0.3/Sea Level optimization).

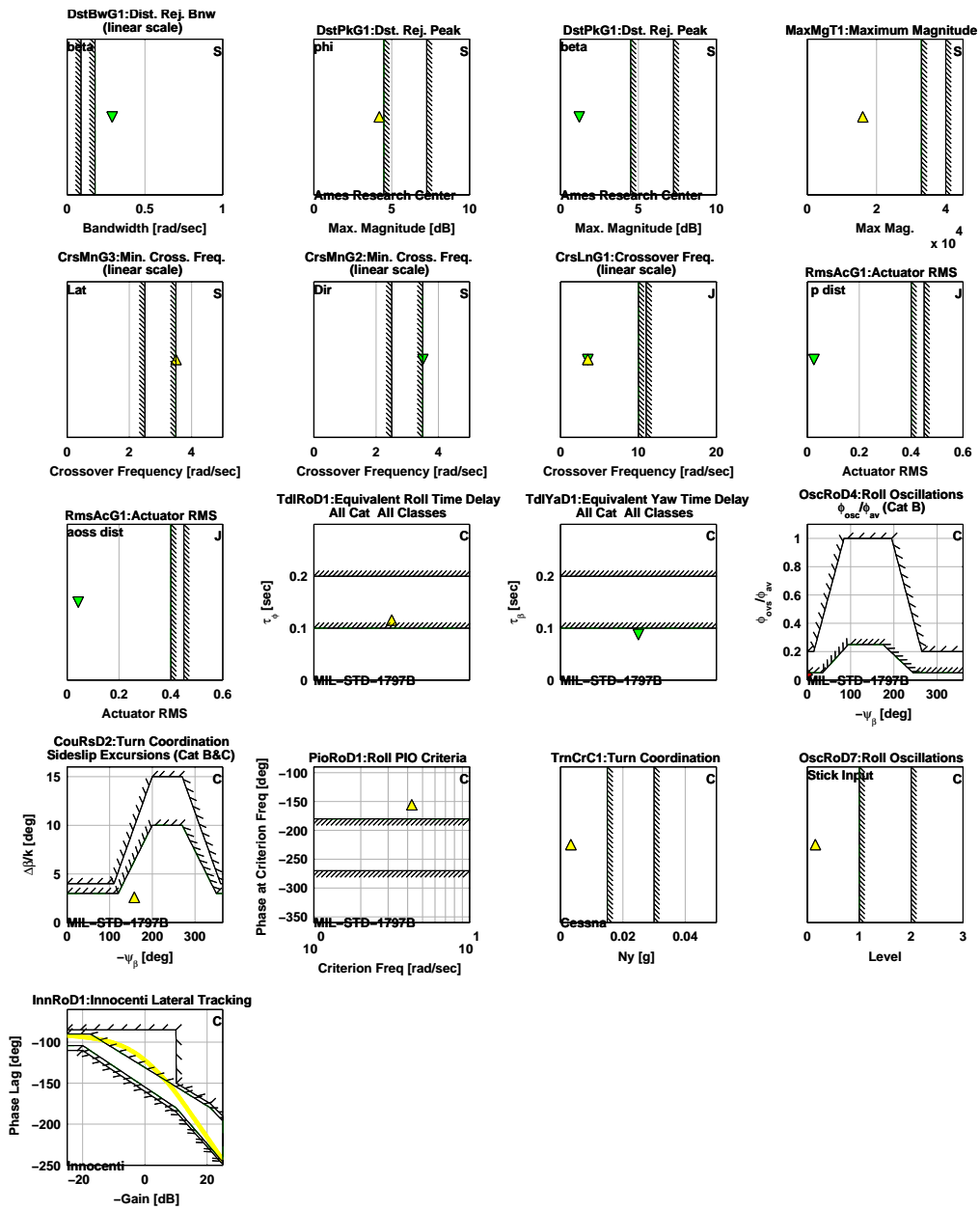


Figure 18. Handling qualities window of the optimized design (2/2) (Mach 0.3/Sea Level optimization).

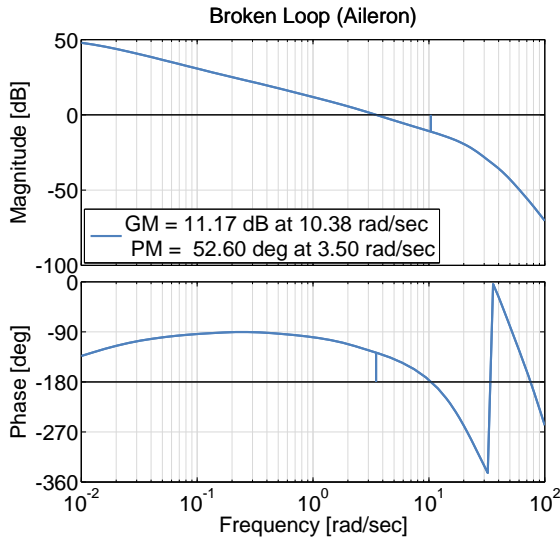


Figure 19. Optimized broken loop (at aileron) response (Mach 0.3/Sea Level flight condition; Nominal weight/CG).

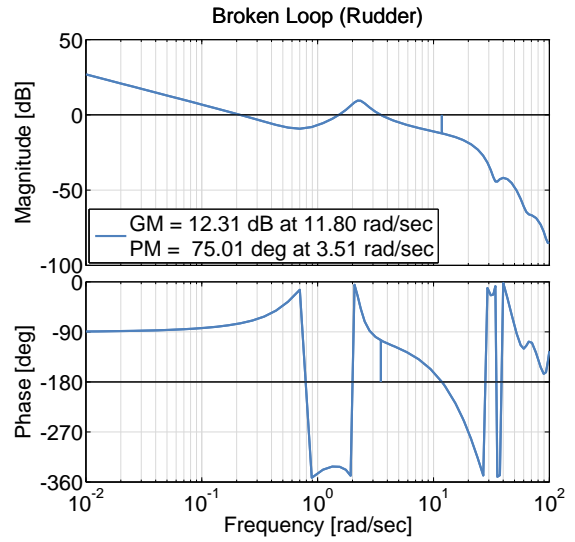


Figure 20. Optimized broken loop (at rudder) response (Mach 0.3/Sea Level flight condition; Nominal weight/CG).

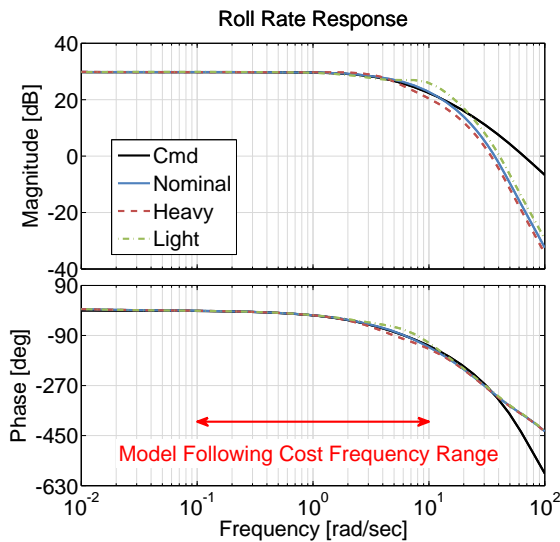


Figure 21. Optimized closed-loop stability axes roll rate response (Mach 0.3/Sea Level flight condition; Nominal, Light, and Heavy loading configurations).

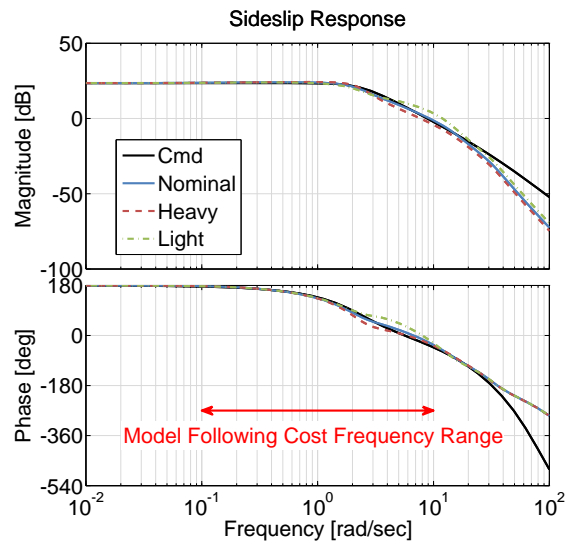


Figure 22. Optimized closed-loop sideslip response (Mach 0.3/Sea Level flight condition; Nominal, Light, and Heavy loading configurations).

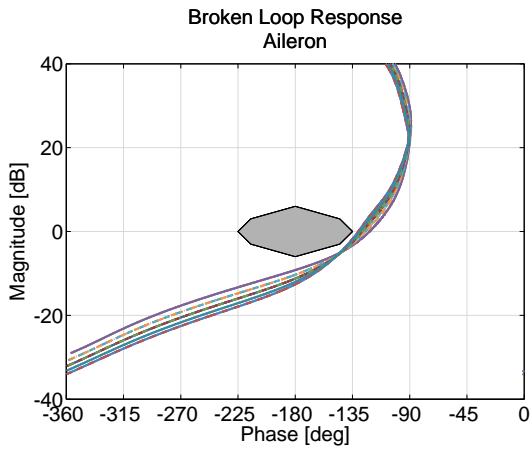


Figure 23. Nichols plot broken at aileron (Mach 0.3/Sea Level flight condition; All weight/CG configurations).

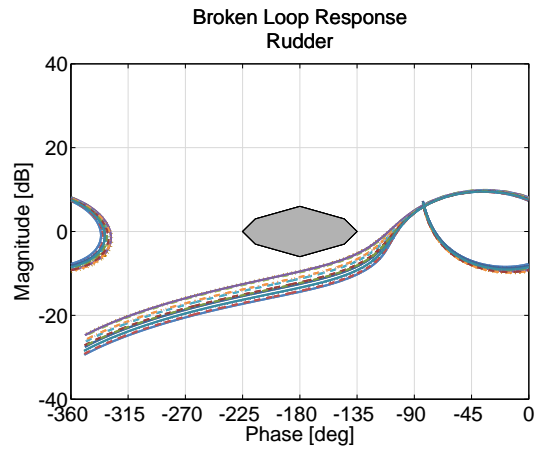


Figure 24. Nichols plot broken at rudder (Mach 0.3/Sea Level flight condition; All weight/CG configurations).

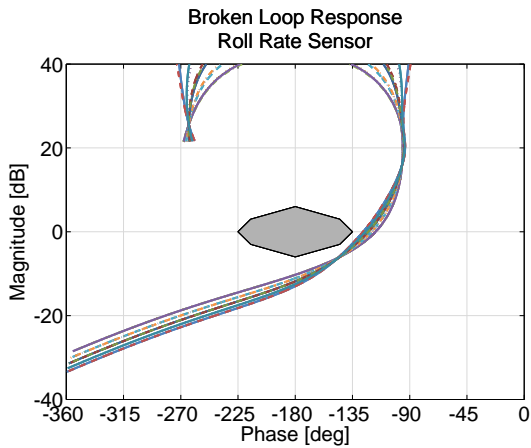


Figure 25. Nichols plot broken at roll rate sensor (Mach 0.3/Sea Level flight condition; All weight/CG configurations).

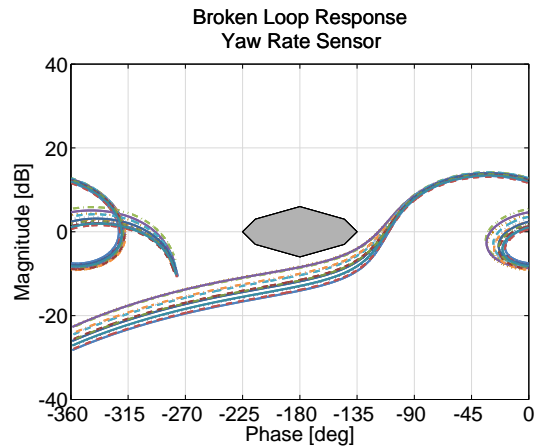


Figure 26. Nichols plot broken at yaw rate sensor (Mach 0.3/Sea Level flight condition; All weight/CG configurations).

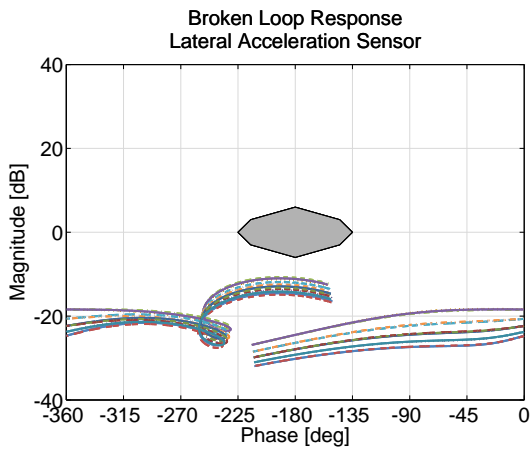


Figure 27. Nichols plot broken at lateral acceleration sensor (Mach 0.3/Sea Level flight condition; All weight/CG configurations).

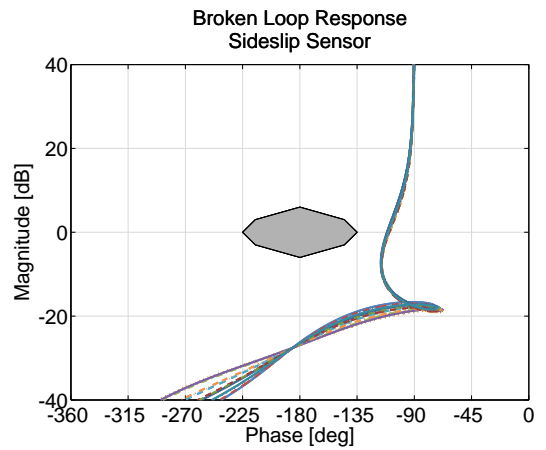


Figure 28. Nichols plot broken at sideslip sensor (Mach 0.3/Sea Level flight condition; All weight/CG configurations).

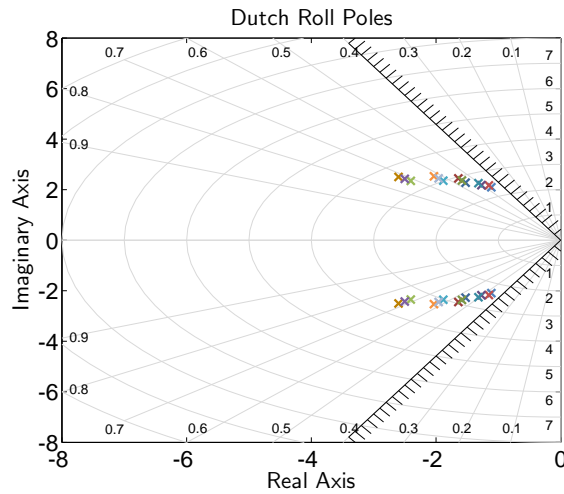


Figure 29. Closed-loop pole locations (Mach 0.3/Sea Level flight condition; All weight/CG configurations).

Figure 30 shows a lateral stick 1-second pulse response of all weight/CG configurations (dotted lines), with the nominal configuration highlighted (solid lines). It shows that the aircraft exhibits a first-order roll rate response, which is expected for a first-order command model. The sideslip response is small, and meets the sideslip excursion specification from MIL-STD-1797B. Figure 31 shows the pedal step response of all weight/CG configurations (dotted lines), with the nominal configuration highlighted (solid lines). The sideslip response is second-order. The off-axis bank angle response can be tailored using the feed-forward cross-feed gains. In this case, the gains were tuned to give about 1 deg of bank angle for 15 deg of sideslip. The gains were also tuned to remove the non-minimum phase characteristic from the roll rate response to rudder deflection.

Figure 32 shows the lateral acceleration response to a 1-cosine sideslip gust of all weight/CG configurations (dotted lines), with the nominal configuration highlighted (solid line). The figure shows that the second peak of the nominal configuration response is smaller in magnitude than the first, which is the load alleviation goal enforced by the sideslip gust specification. More important though, is the direct evaluation of the tail loads shown in Figures 33 through 35.

Figure 33 shows the vertical tail bending moment loads during a rudder kick maneuver. The figure shows the aircraft sideslip (top axis), rudder deflection (middle axis), and tail loads (bottom axis) of all weight/CG configurations (dotted lines), with the nominal configuration highlighted (solid line). The tail loads are well below the maximum tail load described in Section II.B. Additionally, an important characteristic of the rudder deflection response is that the rudder does not change directions (go past zero) upon release of the pedals at time = 5 seconds. This would cause an unacceptable spike in the tail loads, since a rudder deflection to sustain a constant angle of sideslip actually reduces the load on the tail, as evident by the different signs on the β_{cg} and δ_{rud} terms in Equation 4.

Figures 34 and 35 show the vertical tail bending moment loads during a discrete 1-cosine sideslip gust and during extreme turbulence (probability of exceedance = 1×10^{-6}), respectively, for all weight/CG configurations (dotted lines), with the nominal configuration highlighted (solid line). The tail loads are well below the maximum tail load described in Section II.B for all configurations.

Note that only the vertical tail bending moment was considered here for illustrative purposes, however, it is important to look at the trade-off between the three critical tail loads—lateral shear, bending, and torsion.

B. Gain Schedule

With the point design validated, a gain schedule is now determined for the full flight envelope. The results in this section are shown for the nominal weight/CG configurations at each flight condition, unless otherwise noted. However, the strategy of enforcing the stability margin, Nichols margin, and model following cost for the off-nominal weight/CG configurations is still used.

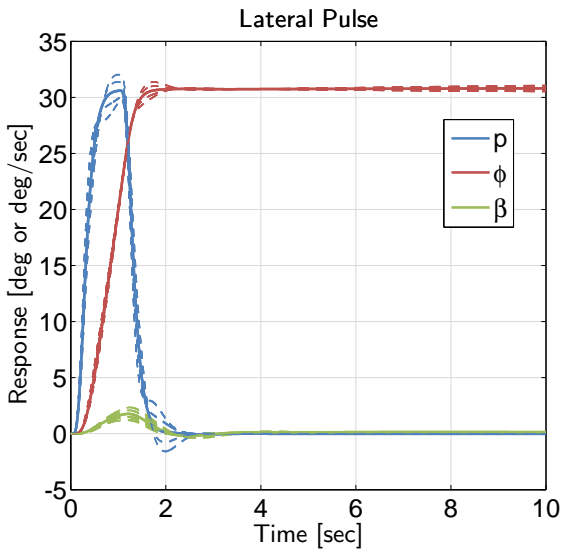


Figure 30. Time history response to a 1-second singlet lateral stick input (Mach 0.3/Sea Level flight condition; All weight/CG configurations).

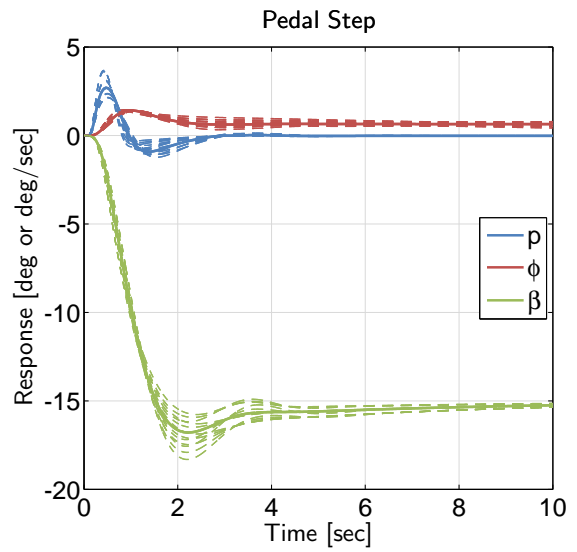


Figure 31. Time history pedal step response (Mach 0.3/Sea Level flight condition; All weight/CG configurations).

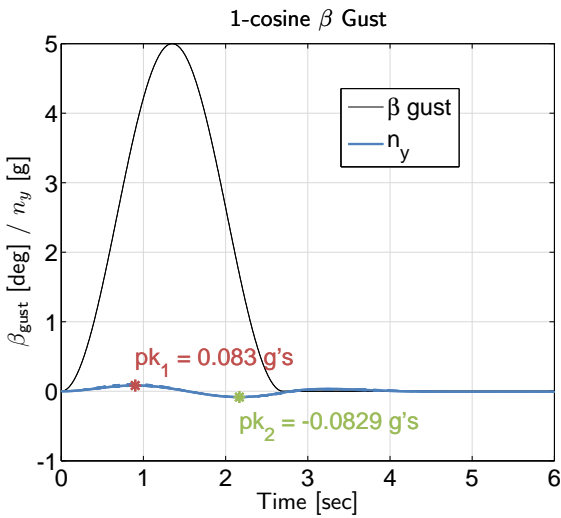


Figure 32. Time history of discrete 1-cosine sideslip gust (Mach 0.3/Sea Level flight condition; All weight/CG configurations).

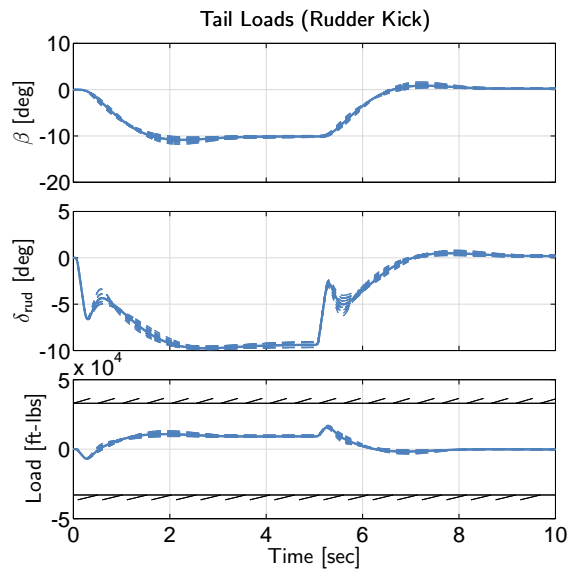


Figure 33. Time history of tail loads during rudder kick maneuver (Mach 0.3/Sea Level flight condition; All weight/CG configurations).

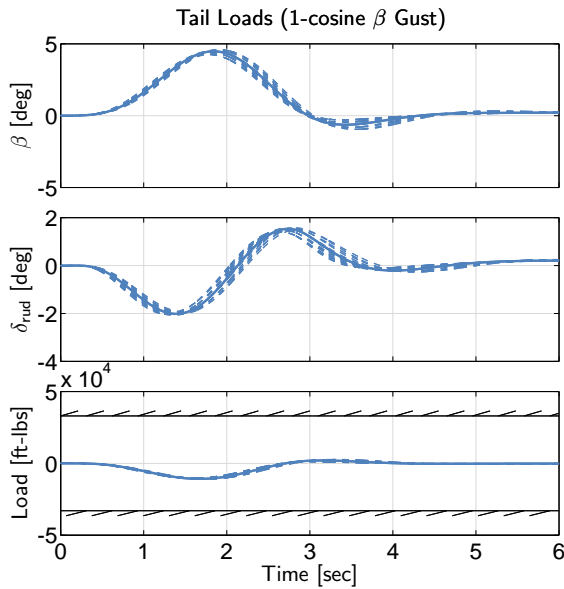


Figure 34. Time history of tail loads during discrete 1-cosine sideslip gust (Mach 0.3/Sea Level flight condition; All weight/CG configurations).

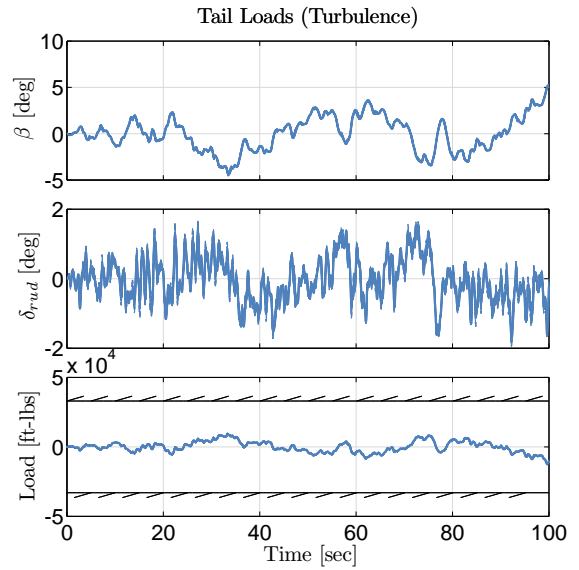


Figure 35. Time history of tail loads under turbulence (Mach 0.3/Sea Level flight condition; All weight/CG configurations).

The gain schedule is determined using CONDUIT[®] Batch mode. Each Batch case (flight condition) is initialized as described in Section VI and optimized. Optimization takes roughly 10 minutes for each Batch case, and the entire gain schedule can be run overnight. Once all cases have been optimized, the gain schedule is implemented as a function of Mach and inverse dynamic pressure, $1/\bar{q}$, (plots are shown as a function of $40/\bar{q}$ for scale). Subsequently, the gain schedule is checked for all flight condition and weight/CG combinations, which takes several hours to run all 858 cases.

Figures 36 and 37 show the gain schedules for the lateral axis feed-forward gains. These gains are primarily functions of the bare-airframe roll mode time constants, as shown in Equations 20 and 21. Figures 38 through 40 show the gain schedules for the directional axis feed-forward gains. These gains are primarily functions of the bare-airframe Dutch roll frequency and damping, as shown in Equations 22 through 24.

Figures 41 and 42 show the gain schedules for the roll rate and integral roll rate feedback gains to the aileron actuator. These gains are primarily driven by the lateral axis crossover frequency and lateral DRB specifications, respectively, and are well grouped for the different Mach numbers, with the integral roll rate gain splitting at the lower dynamic pressures (higher values of $40/\bar{q}$). Figure 43 shows the gain schedule for the roll rate feedback gain to the rudder actuator. This gain is calculated as described in Section VI.B.

Figures 44 through 46 show the gain schedules for the directional feedback gains to the rudder actuator. The sideslip rate feedback gain shown in Figure 44 is well grouped for the different Mach numbers. The sideslip and integral sideslip gains, shown in Figures 45 and 46, respectively, have two smooth regions in their curves, with a nonlinear break at a dynamic pressure of $\bar{q} = 133$ psf ($40/\bar{q} = 0.3$). This is because different specifications drive the optimization in the regions below and above this dynamic pressure. For dynamic pressures lower than $\bar{q} = 133$ psf (values of $40/\bar{q}$ above 0.3), the crossover frequency values are on the $\omega_c \geq 3.5$ rad/sec boundary (Figure 50), and this specification drives the directional axis gains. However, for dynamic pressures greater than $\bar{q} = 133$ psf (values of $40/\bar{q}$ below 0.3), the eigen-damping values are on the $\zeta \geq 0.4$ boundary (Figure 57), and this specification drives the directional axis gains.

Figures 47 and 48 show the gain schedules for the sideslip rate and sideslip feedback gains to the aileron actuator. These gains are determined based on Equations 39 and 40, and are also well grouped for the different Mach numbers. Overall, Figures 36 through 48 show the excellent overall smoothness in the gain trends, which is important when determining a gain schedule.

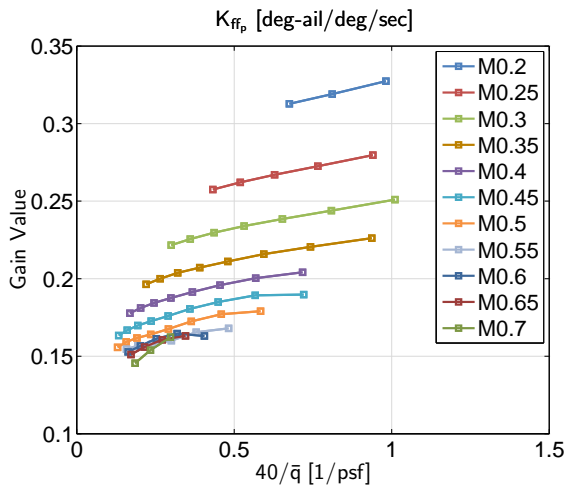


Figure 36. Lateral axis feed forward gain schedule as a function of Mach and inverse dynamic pressure.

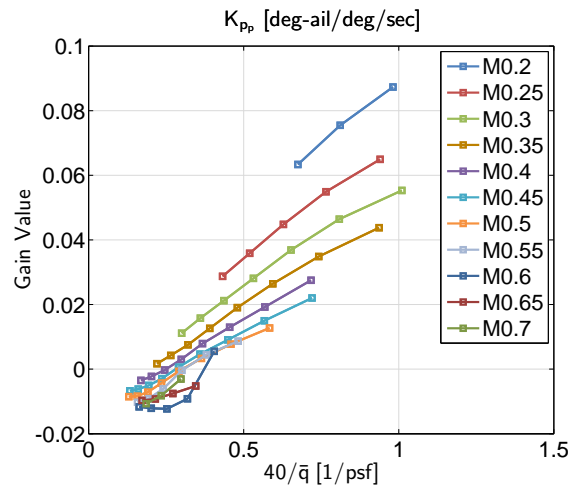


Figure 37. Lateral axis feed forward gain schedule as a function of Mach and inverse dynamic pressure.

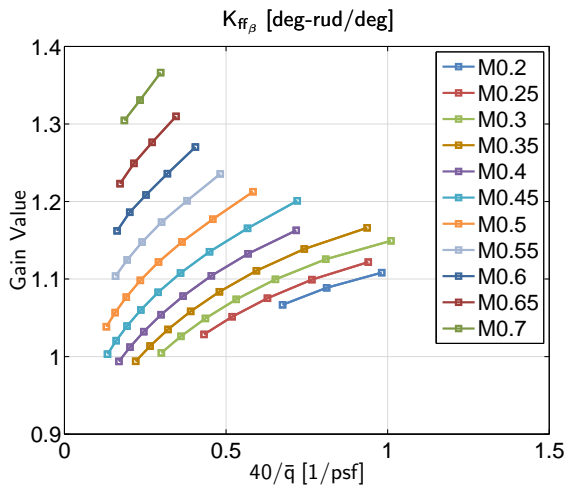


Figure 38. Directional axis feed forward gain schedule as a function of Mach and inverse dynamic pressure.

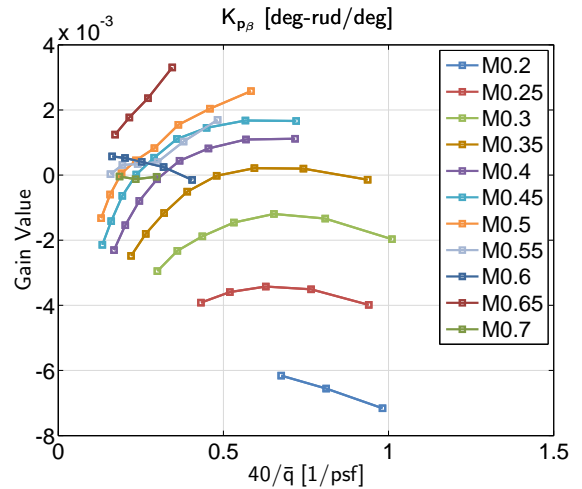


Figure 39. Directional axis feed forward gain schedule as a function of Mach and inverse dynamic pressure.

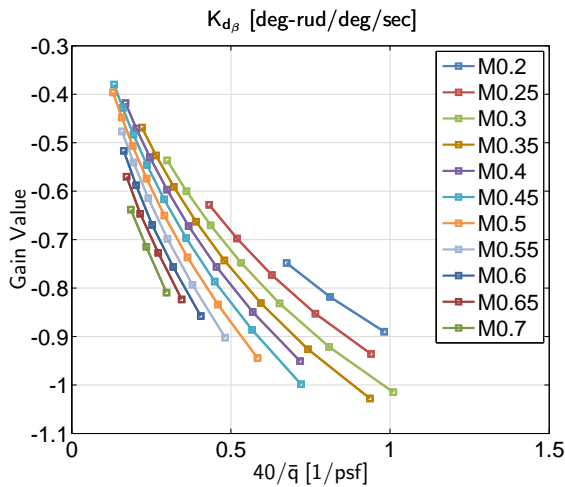


Figure 40. Directional axis feed forward gain schedule as a function of Mach and inverse dynamic pressure.

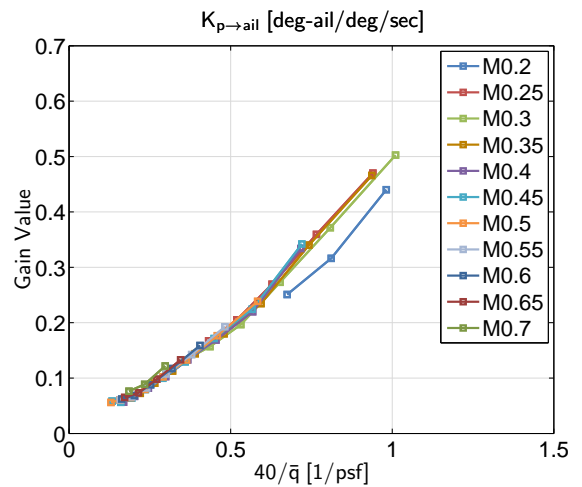


Figure 41. Lateral axis on-axis feedback gain schedule as a function of Mach and inverse dynamic pressure.

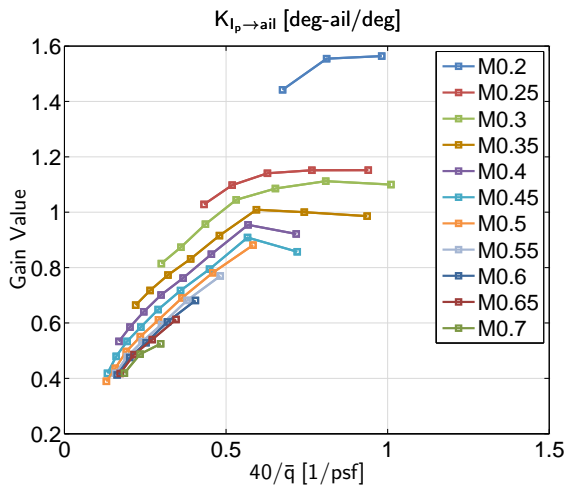


Figure 42. Lateral axis on-axis feedback gain schedule as a function of Mach and inverse dynamic pressure.

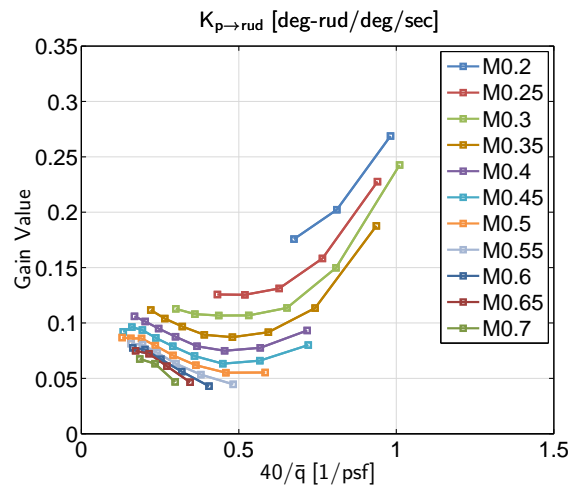


Figure 43. Lateral axis off-axis feedback gain schedule as a function of Mach and inverse dynamic pressure.

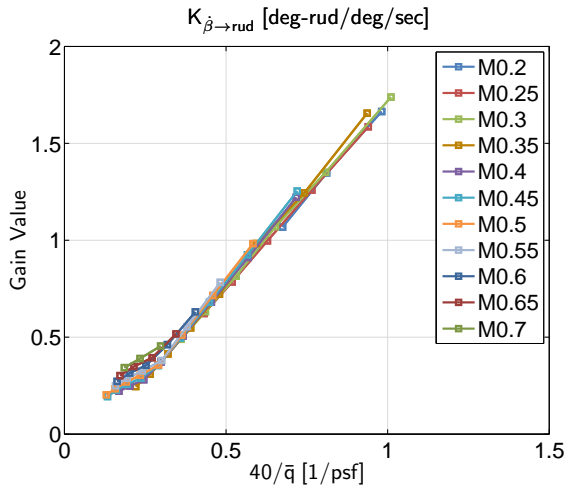


Figure 44. Directional axis on-axis feedback gain schedule as a function of Mach and inverse dynamic pressure.

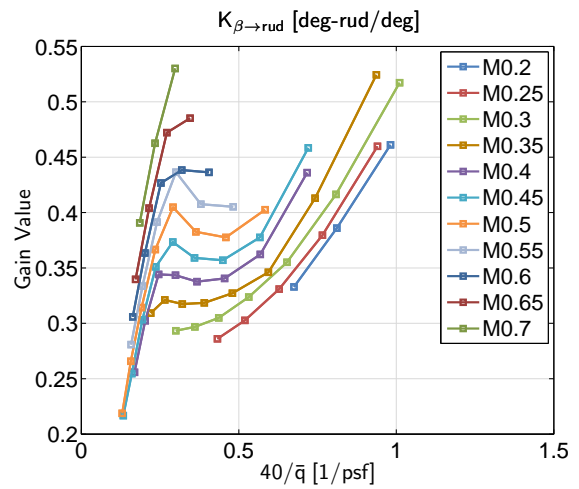


Figure 45. Directional axis on-axis feedback gain schedule as a function of Mach and inverse dynamic pressure.

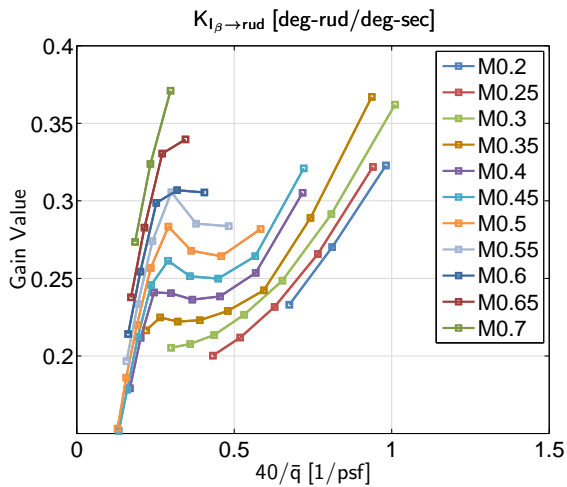


Figure 46. Directional axis on-axis feedback gain schedule as a function of Mach and inverse dynamic pressure.

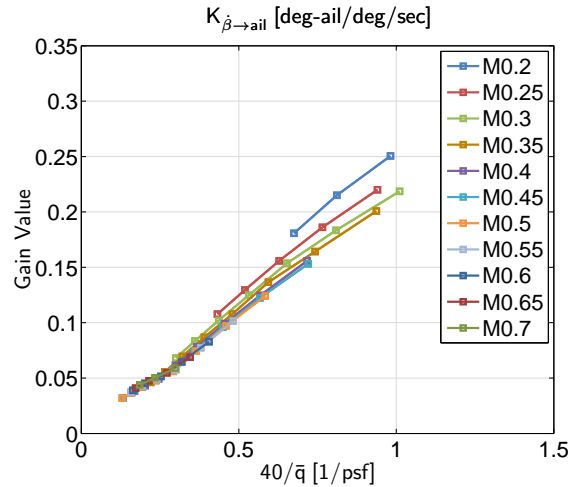


Figure 47. Directional axis off-axis feedback gain schedule as a function of Mach and inverse dynamic pressure.

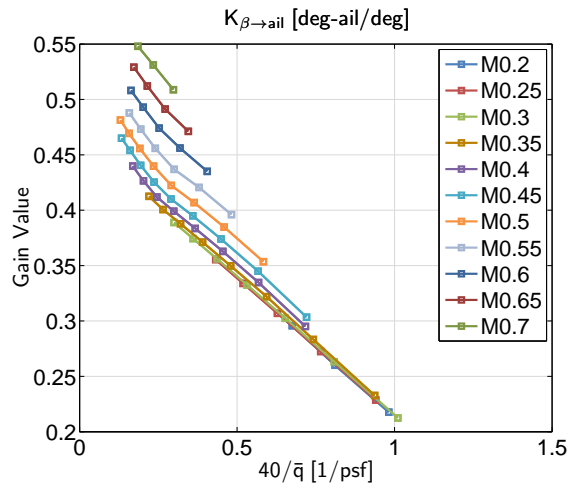


Figure 48. Directional axis off-axis feedback gain schedule as a function of Mach and inverse dynamic pressure.

Figure 49 shows the lateral axis crossover frequency of the nominal weight/CG configurations for all flight conditions. For all flight conditions, the crossover frequency is $\omega_c = 3.5$ rad/sec (due to the optimization strategy of enforcing crossover frequency as both a soft constraint and as a summed objective). Figure 50 shows the directional axis crossover frequency of the nominal weight/CG configurations for all flight conditions. For the higher dynamic pressure cases (low values of $40/\bar{q}$), the crossover frequency is above the minimum enforced value of $\omega_c \geq 3.5$ rad/sec. This optimized solution is reached in order to meet the other specifications, specifically off-nominal model following cost specifications at those flight conditions as well as the minimum damping ratio requirement. Figures 51 and 52 show the broken-loop responses of the nominal configurations for all flight conditions for the loop broken at the aileron actuator and rudder actuator, respectively. Highlighted on the figures is the target crossover frequency $\omega_c = 3.5$ rad/sec.

Nichols plots were used to assess the stability robustness of the gain schedule. Figures 53 and 54 show Nichols plots of the broken loop responses of all flight conditions using all weight/CG configurations, broken at the aileron and rudder actuator, respectively. All of the designs avoid the exclusion zones, suggesting good robust stability.

Figures 55 and 56 show the closed-loop stability axes roll rate and sideslip responses of all flight conditions using the nominal weight/CG configurations, respectively. The responses show the lower-order characteristic of all of the designs.

Figure 57 shows the low-frequency ($\omega \leq 10$ rad/sec) minimum damping ratios of the nominal weight/CG configuration at each flight condition. All damping ratios are above the minimum requirement $\zeta \geq 0.4$, with the higher dynamic pressure cases (low values of $40/\bar{q}$) being directly on the boundary due to the optimization strategy of minimizing crossover frequency and actuator usage (“cost of feedback”). For the lower dynamic pressure cases (high values of $40/\bar{q}$), the damping ratio is greater than the $\zeta = 0.4$ boundary since higher gains were required to meet the minimum crossover frequency requirement, shown in Figure 50.

Figure 58 shows the Dutch roll poles for all weight/CG configurations at all flight conditions. For several of the high dynamic pressure flight conditions (low values of $40/\bar{q}$), where the damping ratio of the nominal weight/CG configurations is $\zeta = 0.4$, there are off-nominal loading configurations with damping ratios lower than $\zeta = 0.4$. However, there are no unacceptably low damping ratios for any of the designs. It is possible to include off-nominal models in the evaluation of the minimum damping ratio specification during optimization to get the associated damping ratios above $\zeta = 0.4$, however this was not done for this analysis.

Figures 59 and 60 show the roll rate and sideslip LOES fit costs for of the nominal weight/CG configuration at each flight condition. For both axes, the designs are below the requirements, indicating that the designs exhibit lower-order response characteristics.

Figure 61 shows the lateral acceleration response to a sideslip gust specification of the nominal weight/CG configuration at each flight condition. As with the low-frequency damping ratio specification, the optimization strategy of minimizing crossover frequency and actuator usage pushed the sideslip gust specification up to the boundary.

Figure 62 shows the peak tail load during rudder kick maneuver for all weight/CG configurations at

each flight condition. The peak tail loads are below the maximum tail load described in Section II.B for all weight/CG configurations at all flight conditions.

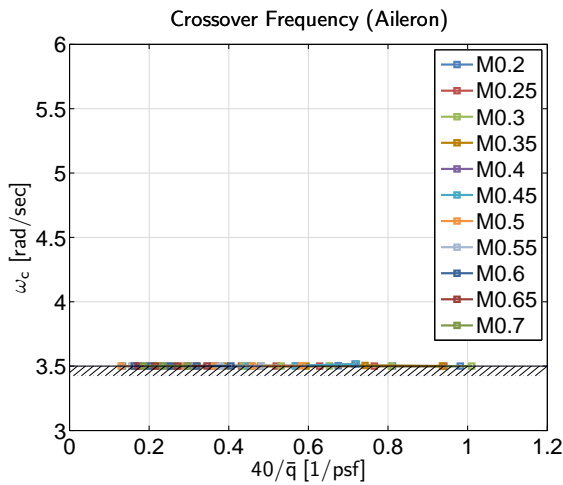


Figure 49. Lateral axis crossover frequency as a function of Mach and inverse dynamic pressure (All flight conditions; Nominal weight/CG).

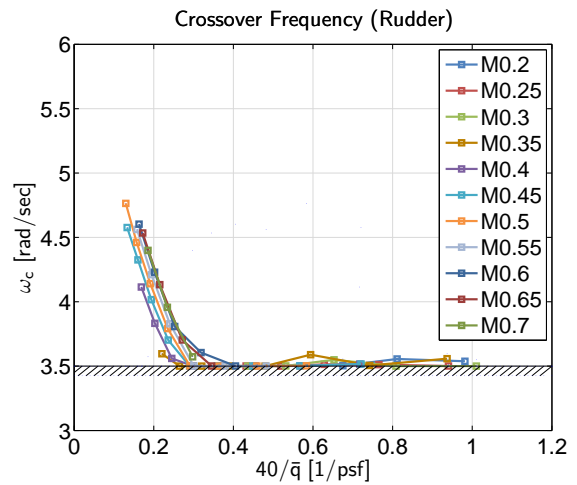


Figure 50. Directional axis crossover frequency as a function of Mach and inverse dynamic pressure (All flight conditions; Nominal weight/CG).

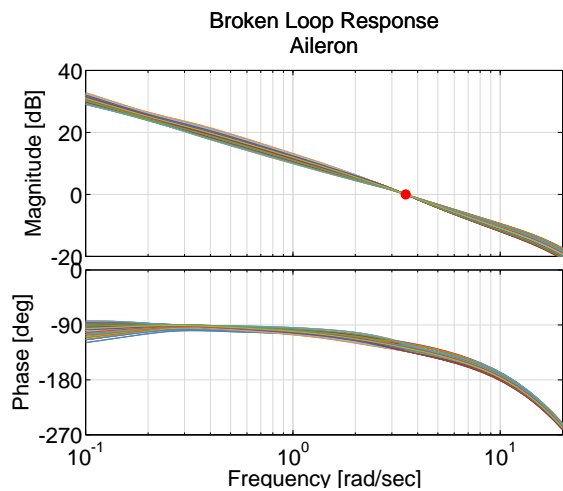


Figure 51. Broken loop (at aileron) frequency response (All flight conditions; Nominal weight/CG).

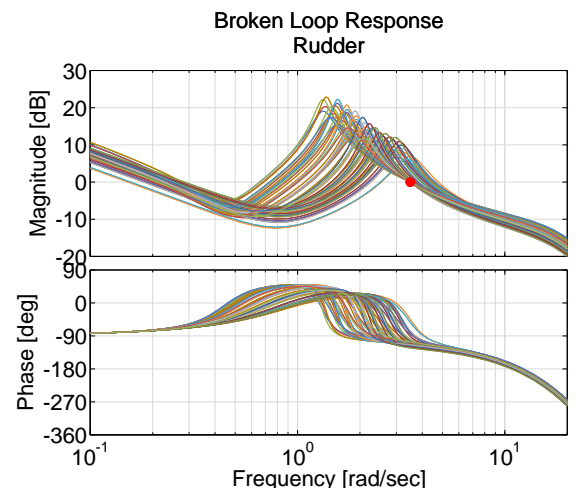


Figure 52. Broken loop (at rudder) frequency response (All flight conditions; Nominal weight/CG).

Figure 63 shows the lateral acceleration for all weight/CG configurations at all flight conditions during a 30 deg banked turn. Plotted on the lateral acceleration axis are the ± 0.015 g boundaries for turn coordination described in Section V.B. All of the designs meet this Second Tier steady-state turn coordination requirement, which is not included in the optimization process, validating the ratio chosen to constrain the integral sideslip gain (Equation 35).

Figure 64 shows the sideslip excursions values of all nominal configurations at every flight condition and associated specification boundaries. This is also a Second Tier specification, not included in the optimization process. This specification is primarily a function of the off-axis sideslip and sideslip rate feedback to aileron gains, which are determined based on Equations 39 and 40. The specification is met for all of the nominal weight/CG configurations, suggesting good selection of the off-axis gains.

Figure 65 shows the closed-loop roll rate responses of all configurations and all flight conditions plotted on the Innocenti criteria. This is also a Second Tier requirement, which is met for the majority of the designs, suggesting sufficient overlap between this specification and the First Tier specifications.

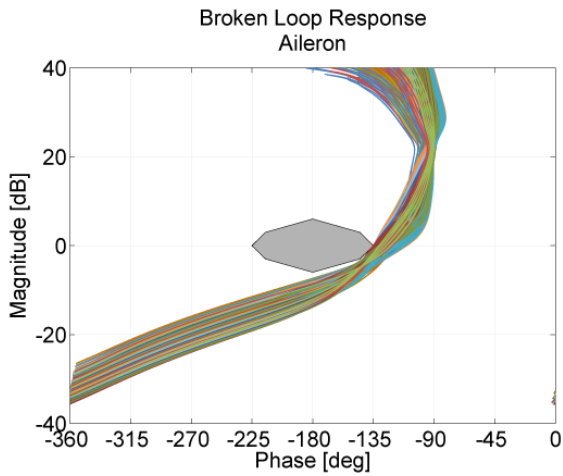


Figure 53. Broken loop (at aileron) Nichols plot (All flight conditions; All weight/CG).

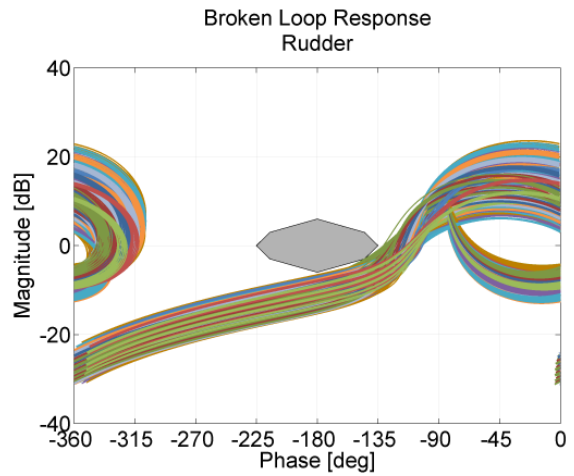


Figure 54. Broken loop (at rudder) Nichols plot (All flight conditions; All weight/CG).

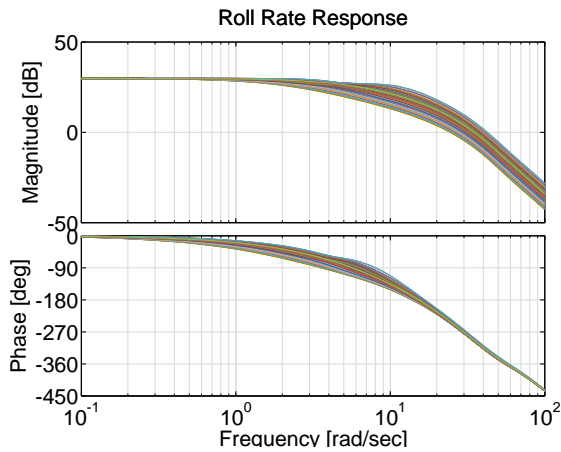


Figure 55. Closed-loop stability axes roll rate response (All flight conditions; Nominal weight/CG).

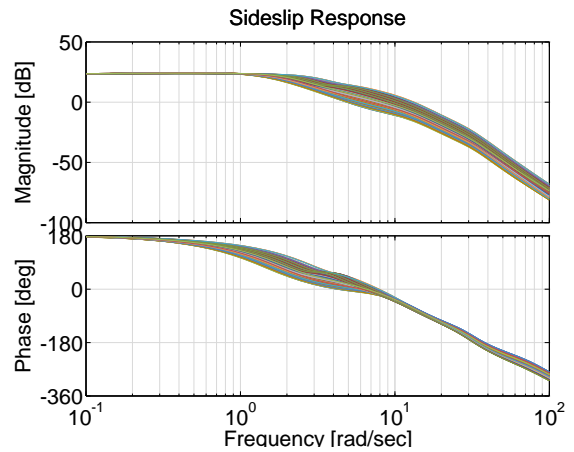


Figure 56. Closed-loop sideslip response (All flight conditions; Nominal weight/CG).

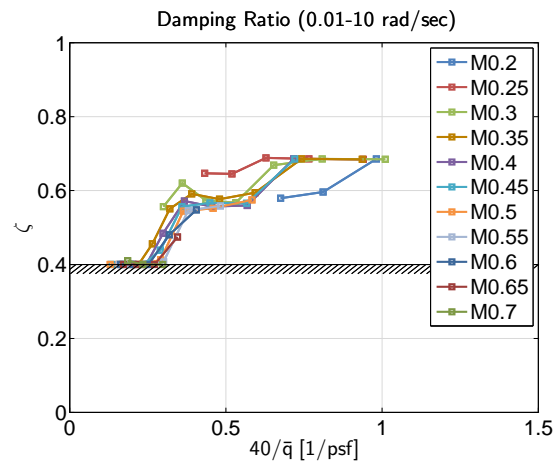


Figure 57. Eigen damping of low-frequency modes as a function of Mach and inverse dynamic pressure (All flight conditions; Nominal weight/CG).

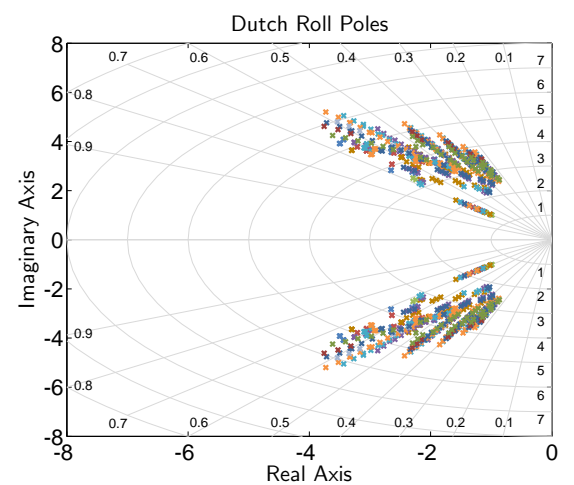


Figure 58. Closed-loop pole locations (All flight conditions; All weight/CG configurations).

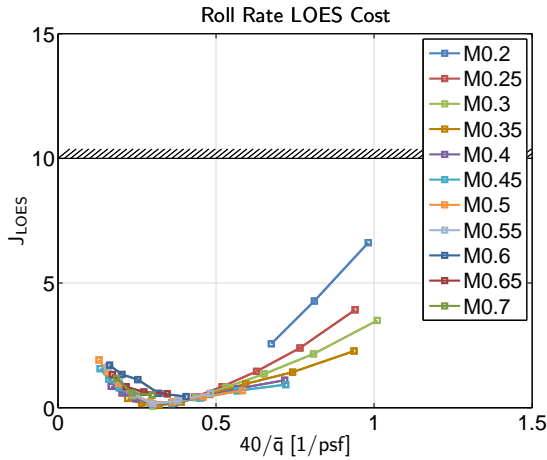


Figure 59. Roll rate response LOES cost as a function of Mach and inverse dynamic pressure (All flight conditions; Nominal weight/CG).

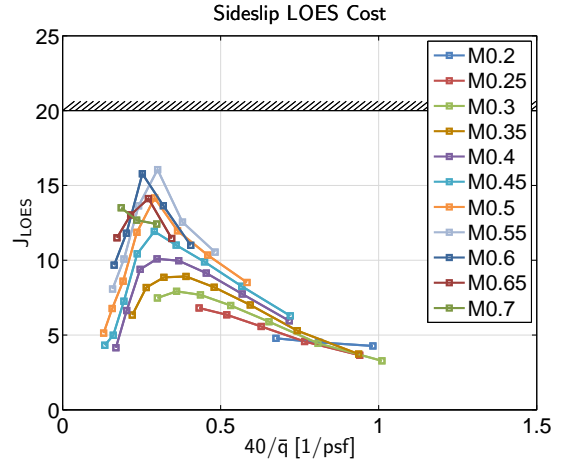


Figure 60. Sideslip response LOES cost as a function of Mach and inverse dynamic pressure (All flight conditions; Nominal weight/CG).

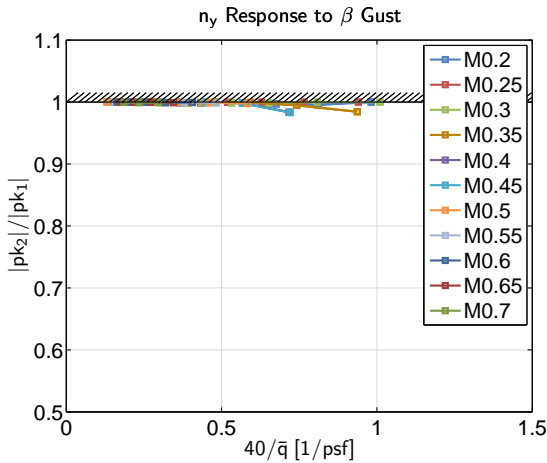


Figure 61. Sideslip gust response as a function of Mach and inverse dynamic pressure (All flight conditions; Nominal weight/CG).

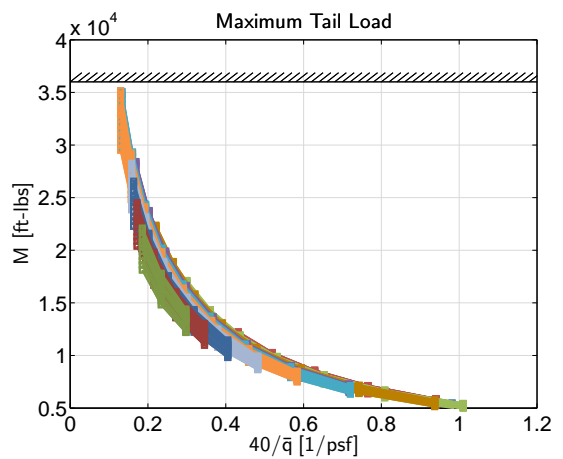


Figure 62. Maximum vertical tail load as a function of Mach and inverse dynamic pressure (All flight conditions; All weight/CG).

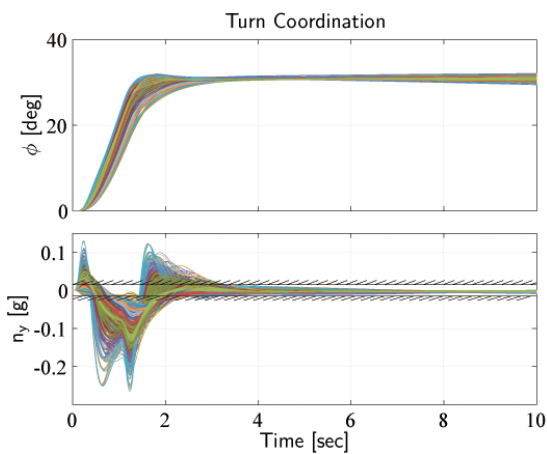


Figure 63. Steady state turn coordination (All flight conditions; All weight/CG configurations).

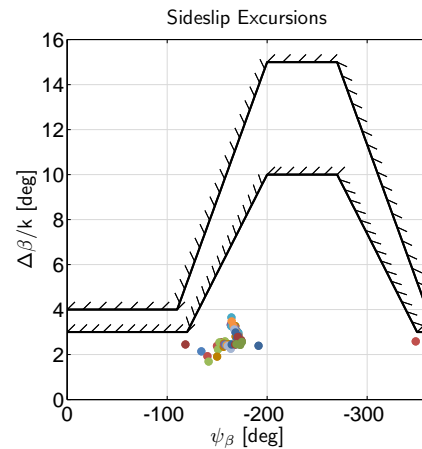


Figure 64. All flight conditions plotted on the sideslip excursions criteria (All flight conditions; Nominal weight/CG).

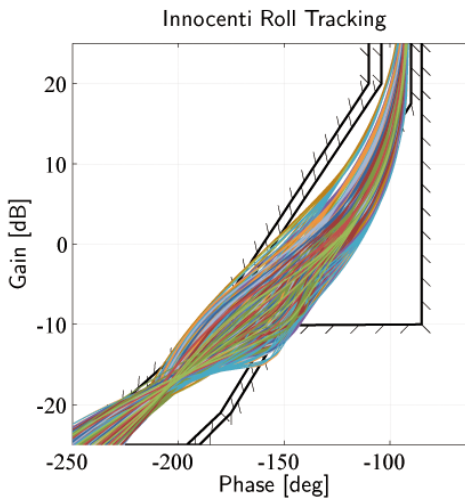


Figure 65. All flight conditions plotted on the Innocenti Lateral Tracking criteria (All flight conditions; All weight/CG).

VIII. Conclusions

1. Feed-forward gains were explicitly determined to achieve good handling qualities by exploiting the parallels between the commonly used fixed-wing control laws investigated in this study and an explicit model following architecture.
2. The LQR design method was utilized in a preliminary design phase to initialize the gains for the follow-on CONDUIT[®] multi-objective optimization. This proved very useful as a starting condition for the optimization with nearly all of the specifications being met. Using LQR in preliminary design also helps determine which feedback gains are sensitive and which can be dropped from the control laws.
3. Cross-feed gains were used in both the feed-forward and feedback paths. In the feedback path, sideslip and sideslip rate were fed back to the aileron to help decouple the roll and yaw responses. The feedback gains of sideslip and sideslip rate to aileron were analytically determined to achieve the desired roll and yaw decoupling. In the feed-forward path, cross-feed gains were used to tune the off-axis responses of the aircraft. This allowed tuning of the roll response to pedal input, an important handling qualities trait.
4. The multi-objective optimization method employed in this study proved capable in determining designs which concurrently meet a large number of frequency- and time-domain specifications for both nominal and off-nominal models, while minimizing over-design (i.e., most economical use of actuators and noise sensitivity). Second Tier requirements were met by designs that were optimized for the First Tier requirements.
5. The multi-model optimization approach used here allowed scheduling with Mach and dynamic pressure only to meet the requirements for the range of weight/CG configurations. Furthermore, using both LQR in preliminary design and a multi-objective optimization method to meet the specifications provided the ability to optimize an entire gain schedule with no manual tuning or iterations, and resulted in a smooth gain schedule.
6. A simple vertical tail bending moment model was developed to demonstrate the importance of tail load considerations in lateral/directional control law design. The next step in the development of the control laws presented in this paper would be to perform a high fidelity aeroservoelasticity loads analysis in order to confirm that all the vertical tail loads stay within the appropriate bounds.

References

- ¹Berger, T., Tischler, M. B., Hagerott, S. G., Gangsaas, D., and Saeed, N., "Longitudinal Control Law Design and Handling Qualities Optimization for a Business Jet Flight Control System," presented at the AIAA Atmospheric Flight Mechanics Conference, Minneapolis, MN, August 2012.
- ²Anon., "Flight Control Design - Best Practices," NATO RTO-TR-029, December 2000.
- ³Pratt, R. W., "Flight Control Systems," AIAA Progress in Astronautics and Aeronautics, Vol. 184, 2000.
- ⁴Gangsaas, D., Hodgkinson, J., Harden, C., Saeed, N., and Chen, K., "Multidisciplinary Control Law Design and Flight Test Demonstration on a Business Jet," presented at the AIAA Guidance, Navigation, and Control Conference and Exhibit, Honolulu, HI, August 2008.
- ⁵Anemaat, W. A. J. and Kaushik, B., "Geometry Design Assistant for Airplane Preliminary Design," presented at the AIAA Aerospace Sciences Meeting, Orlando, FL, January 2011.
- ⁶Anon., "Type Certificate Data Sheet No. A1WI Rev. 19," Department of Transportation Federal Aviation Administration, 2011.
- ⁷Tischler, M. B. and Remple, R. K., *Aircraft and Rotorcraft System Identification: Engineering Methods and Flight Test Examples Second Edition*, AIAA, 2012.
- ⁸McCormick, B. W., *Aerodynamics, Aeronautics, and Flight Mechanics Second Edition*, Wiley, 1994.
- ⁹Adams, R. J., Buffington, J. M., Sparks, A. G., and Banda, S. S., *Robust Multivariable Flight Control*, Springer-Verlag, 1994.
- ¹⁰Blight, J. D., Calderia, F. R., and Gangsaas, D., "Control Law Development for Aircraft An Example of Industry Practices," presented at the American Control Conference, Seattle, WA, June 2008.
- ¹¹Tischler, M. B., Fletcher, J. W., Morris, P. M., and Tucker, G. E., "Flying Quality Analysis and Flight Evaluation of a Highly Augmented Combat Rotorcraft," *Journal of Guidance, Control, and Dynamics*, Vol. 14, No 5, pp. 954-964, September-October 1991.
- ¹²Tischler, M. B., "Digital Control of Highly Augmented Combat Rotorcraft," NASA-TM-88346, May 1987.
- ¹³Anon., "Flight Control Systems - Design, Installation And Test Of Piloted Aircraft, General Specification For," MIL-DTL-9490E, Department of Defense, April 2008.
- ¹⁴Anon., "Airworthiness Standards: Transport Category Airplanes," Code of Federal Regulations, Title 14, Part 25, Department of Transportation Federal Aviation Administration, January 2004.
- ¹⁵Anon., "Flying Qualities of Piloted Aircraft," MIL-STD-1797B, Department of Defense Interface Standard, February 2006.
- ¹⁶Tischler, M. B., Lee, J. A., and Colbourne, J. D., "Optimization and Comparison of Alternative Flight Control System Design Methods Using a Common Set of Handling-Qualities Criteria," presented at the AIAA Guidance, Navigation, and Control Conference, Montreal, Canada, August 2001.
- ¹⁷Tischler, M. B., Ivler, C. M., Mansur, M. H., Cheung, K. K., Berger, T., and Berrios, M., "Handling-Qualities Optimization and Trade-offs in Rotorcraft Flight Control Design," presented at the Rotorcraft Handling Qualities Conference, University of Liverpool, UK, November 2008.
- ¹⁸Duda, H., "Prediction of Pilot-in-the-Loop Oscillations Due to Rate Saturation," *Journal of Guidance, Navigation, and Control*, Vol. 20, No. 3, May-June 1997.
- ¹⁹Blanken, C. L., Hoh, R. H., Mitchell, D. G., and Key, D. L., "Test Guide for ADS-33E-PRF," US Army RDECOM special report AMR-AF-08-07, July 2008.
- ²⁰Innocenti, M. and Thukral, A., "Roll Performance Criteria for Highly Augmented Aircraft," *Journal of Guidance, Navigation, and Control*, Vol. 14, No. 6, November-December 1991.
- ²¹Mansur, M. H. and Tischler, M. B., "Flight Test Comparison of Alternate Strategies for Multi-Loop Control Law Optimization," presented at the American Helicopter Society 69th Annual Forum, Phoenix, AZ, May 2013.
- ²²Magni, J. F., Bennani, S., and Terlouw, J., *Robust Flight Control: A Design Challenge*, Springer Verlag, Lecture Notes in Control and Information Sciences, number 224, 1997.